
Electronic Theses and Dissertations, 2004-2019

2015

A Multi-Scale CFD Analysis of Patient-Specific Geometries to Tailor LVAD Cannula Implantation Under Pulsatile Flow Conditions: an investigation aimed at reducing stroke incidence in LVADs

Ray Prather
University of Central Florida



Part of the [Mechanical Engineering Commons](#)

Find similar works at: <https://stars.library.ucf.edu/etd>

University of Central Florida Libraries <http://library.ucf.edu>

This Masters Thesis (Open Access) is brought to you for free and open access by STARS. It has been accepted for inclusion in Electronic Theses and Dissertations, 2004-2019 by an authorized administrator of STARS. For more information, please contact STARS@ucf.edu.

STARS Citation

Prather, Ray, "A Multi-Scale CFD Analysis of Patient-Specific Geometries to Tailor LVAD Cannula Implantation Under Pulsatile Flow Conditions: an investigation aimed at reducing stroke incidence in LVADs" (2015). *Electronic Theses and Dissertations, 2004-2019*. 1167.

<https://stars.library.ucf.edu/etd/1167>



**A MULTI-SCALE CFD ANALYSIS OF PATIENT-
SPECIFIC GEOMETRIES TO TAILOR LVAD
CANNULA IMPLANTATION UNDER PULSATILE
FLOW CONDITIONS: AN INVESTIGATION
AIMED AT REDUCING STROKE INCIDENCE IN
LVADS**

by

RAY PRATHER

B.S.M.E. University of Central Florida, 2013

A thesis submitted in partial fulfillment of the requirements
for the degree of Master of Science
in the Department of Mechanical and Aerospace Engineering
in the College of Engineering and Computer Science
at the University of Central Florida
Orlando, Florida

Spring Term
2015

Major Professor: Alain Kassab

© 2015 Ray Otto Prather

ABSTRACT

A Left Ventricular Assist Device (LVAD) is a mechanical pump that provides temporary circulatory support when used as bridge-to-transplantation and relieves workload demand placed on a failing heart allowing for myocardia recovery when used as destination therapy. Stroke is the most devastating complication after ventricular assist device (VAD) implantation, with an incidence of 14-47% over 3-6 months, despite improvements in device design and anticoagulation. This complication due to thrombus formation and subsequent transport through the vasculature to cerebral vessels continues to limit the widespread implementation of VAD therapy. Patient-specific computational fluid dynamics (CFD) analysis may elucidate ways to reduce this risk.

A multi-scale model of the aortic circulation was employed to examine the effects on flow conditions resulting from varying the VAD cannula implantation location and angle of incidence of the anastomosis to the ascending aorta based on a patient-specific geometry obtained from CT scans. The purpose of this study is to numerically investigate tailoring cannula implantation with the aim of reducing the number of thrombi reaching cerebral vessels (vertebral and carotid arteries), thereby reducing incidence of stroke in LVADs. The multi-scale computation consists of a 0D lumped parameter model (LPM) of the circulation modeled via a 50 degree of freedom (DOF) electrical circuit analogy that includes an LVAD model coupled to a 3D computational fluid dynamics model of the circulation. An in-house adaptive Runge-Kutta method is utilized to solve the 50 DOF LPM, and the StarCCM+ CFD code is utilized to solve the flow field. This 0D-3D coupling for the flow is accomplished iteratively with the 0D LPM providing the pulsatile boundary conditions that drive the 3D CFD time-accurate computations

of the flow field. The 0D-3D computations are carried out in a parallel environment on a multi-node cluster computational platform. Investigated angle configurations include cannula implantations at 60° and 90° to the right lateral wall of the ascending aorta. We also considered placements of the VAD cannula along the ascending aorta in which distances of the VAD anastomosis is varied relative to the takeoff of the innominate artery. We implemented a mixed Eulerian-Lagrangian particle-tracking scheme to quantify the number of stroke-inducing particles reaching cerebral vessel outlets and included flow visualization through streamlines to identify regions of strong vorticity and flow stagnation, which can promote thrombus formation. Thrombi were modeled as spheres with perfectly elastic interactions numerically released randomly in time and space at cannula inlet plane. Based on clinical observation of the range of thrombus sizes encountered in such cases, particle diameters of 2.0mm, 3.0mm and 5.0mm were investigated in our numerical computations. Pulsatile flow results for aforementioned angles suggest that a 90° cannula implementation causes flow impingement on the left lateral aortic wall and appears to be highly thrombogenic due to large momentum losses and zones of large recirculation and that shallow and intermediate cannula angles promote more regular flow carrying particles towards the lower body potentially reducing stroke risk. Results are presented from this detailed study accompanied with statistical analysis of the significance of stroke risk reduction under various implantation scenarios. Indications from this pulsatile numerical study suggest that up to a 50% reduction in stroke rate can be achieved with tailoring of cannula implantation. Results are consistent with significant reduction in stroke incidence achieved by tailoring cannula implantation as reported in previous steady flow computations carried out by our group.

As such, results of this study suggest that a simple surgical maneuver in the process of VAD implantation may significantly improve patient life.

ACKNOWLEDGMENTS

I thank my advisor Dr. Alain Kassab, for his guidance and support throughout this project. For his extensive understanding of fluid mechanics and numerical methods proved to be of great help. The undying support of my father and mother, who relentlessly sustained me. The great assistance provided by my co-workers Marcus Ni and Nicholas Voce whose programming skills were of great use.

TABLE OF CONTENTS

LIST OF FIGURES	x
LIST OF TABLES	xii
ABBREVIATIONS	xiii
1 CHAPTER 1: INTRODUCTION.....	1
1.1 Vascular Organization.....	3
1.2 Vascular Diseases	5
1.2.1 Heart Failure.....	5
1.2.2 Thrombosis Induced Stroke	6
1.3 Modeling.....	6
1.3.1 Patient Specific Geometries	6
1.3.2 Boundary Conditions.....	7
1.3.3 FSI Coupled with CFD	7
1.3.4 Lagrangian Method to Track Microscopic Particulate Flow	8
1.4 Applications.....	9
2 CHAPTER 2: PROBLEM SET UP	11
2.1 Lumped Parameter Model.....	12
2.2 Circulatory System Model.....	14
2.2.1 Step 1: Left Heart.....	15
2.2.2 Step 2: CFD	18
2.2.3 Step 3: Arterial and Venus Beds.....	20

2.2.4	Step 4: Right Heart.....	23
2.2.5	Step 5: Pulmonary System.....	24
2.2.6	Step 6: LVAD	25
2.2.7	Model Tuning.....	28
2.3	Generating System of Differential Equations.....	29
2.4	Solver	32
2.5	CFD Simulation.....	33
2.5.1	Fluid Domain	33
2.5.2	Particles.....	36
2.6	Coupling.....	37
2.7	Statistical method.....	39
3	CHAPTER 3: RESULTS	41
3.1	LPM Outputs	41
3.2	Flow Field Convergence.....	43
3.2.1	Shift up geometry	43
3.2.2	Perpendicular geometry	47
4	CHAPTER 4: DISCUSSION OF PARTICLE TRACKING RESULTS.....	51
5	CHAPTER 5	56
5.1	Conclusion.....	56
5.2	Future Work.....	56
	APPENDIX A: EQUATIONS.....	58

APPENDIX B: FIGURES.....	65
APPENDIX C: TABLES.....	67
APPENDIX D: CODES.....	72
LIST OF REFERENCES.....	79

LIST OF FIGURES

Figure 1 - (a) LVAD implantation, (b) LVAD thoracic location	2
Figure 2 - Circulatory system	3
Figure 3 - Aortic arch and branching vessels (Layton, et al. 2006).....	4
Figure 4 - Blood cloths generation by arteriosclerotic plaques and blood cloths.....	6
Figure 5 - Basic circulatory circuit element.....	13
Figure 6 - Elastance function waveform.....	16
Figure 7 - Heart circuit scheme.....	17
Figure 8 - CFD circuit scheme.....	18
Figure 9 - Arterial and venous beds circuit scheme.....	20
Figure 10 - 180° out of phase waveforms.....	23
Figure 11 - Closed loop circuit for LVAD implementation, G. Fargallah (et al.).....	26
Figure 12 - Hydraulic analogy	29
Figure 13 - LVAD circuit LPM	32
Figure 14 - Patient specific geometries with LVAD configurations	33
Figure 15 - Monitor crosssection in CFD domain (left) and a close up of the upper aortic arch (right)	35
Figure 16 - Injection grid at the base of the inlet cannula	36
Figure 17 - Particle injection at LVAD inlet	37
Figure 18 - Coupling loop work flow	38
Figure 19 - Normal distribution bell curve	40

Figure 20 – In vivo pressure waveforms for left ventricle and aorta by Adam R. Travis et. al [11]	42
.....	42
Figure 21 - Pressure and flow rate waveform generated by LPM	42
Figure 22 - AO cross-section monitor plane.....	43
Figure 23 - AO averaged mass flow rate per iteration in shifted-up LVAD	44
Figure 24 - Streamlines representation through one heart cycle.....	45
Figure 25 - Vector flow field representation through one cycle.....	46
Figure 26 - Cardiac cycle.....	46
Figure 27 - AO averaged mass flow rate per iteration in perpendicular LVAD.....	47
Figure 28 - Streamlines representation through one heart cycle.....	48
Figure 29 - Vector flow field representation though one heart cycle	49
Figure 30 - Cardiac cycle.....	49
Figure 31 - Stagnation point migration through systolic phase	53
Figure 32 - Cardiac cycle.....	53
Figure 33 - FULL LVAD circuit LPM	66

LIST OF TABLES

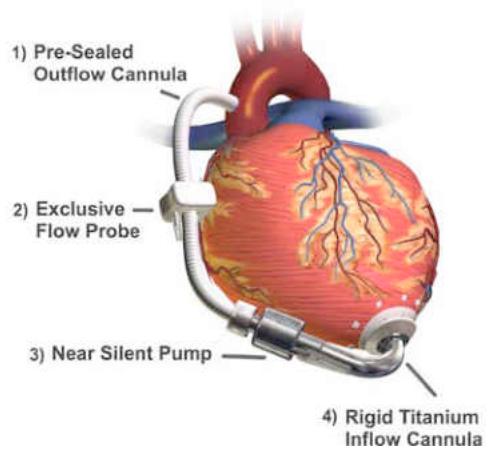
Table 1 - Model operational parameters	12
Table 2 - Left heart parameters.....	17
Table 3 - CFD domain resistance parameters [mmHg s mL ⁻¹] for 4-1 LVAD-AO flow ratios ...	19
Table 4 - Parameters of arterial and venous beds at CFD outlets for 4-1 LVAD-AO flow ratio.	21
Table 5 - Right heart parameters.....	24
Table 6 - Cardio vascular model parameters	27
Table 7 - LVAD parameters	27
Table 8 - Variable in cardio vascular model.....	28
Table 9 - Definition of BC at each boundary.....	41
Table 10 - Percentages of particle entering cerebral vessels	51
Table 11 - Testing criteria for null hypothesis $\mu_1 - \mu_2 = 0$	51
Table 12 - Z-score of mean comparison between steady and transient models.....	52
Table 13 - 3.5mm particle data for Ascending Aorta in the perpendicular geometry	54
Table 14 - 2.5mm particle data for each outlet for Intermediate geometry	68
Table 15 - 2.5mm particle count at cerebral vessels for Intermediate geometry	68
Table 16 - 3.5mm particle data for each outlet for Intermediate geometry	69
Table 17 - 3.5mm particle count at cerebral vessels for Intermediate geometry	69
Table 18 - 2.5mm particle count at each outlet for Perpendicular geometry.....	70
Table 19 - 2.5mm particle count at cerebral vessels for Perpendicular geometry	70

ABBREVIATIONS

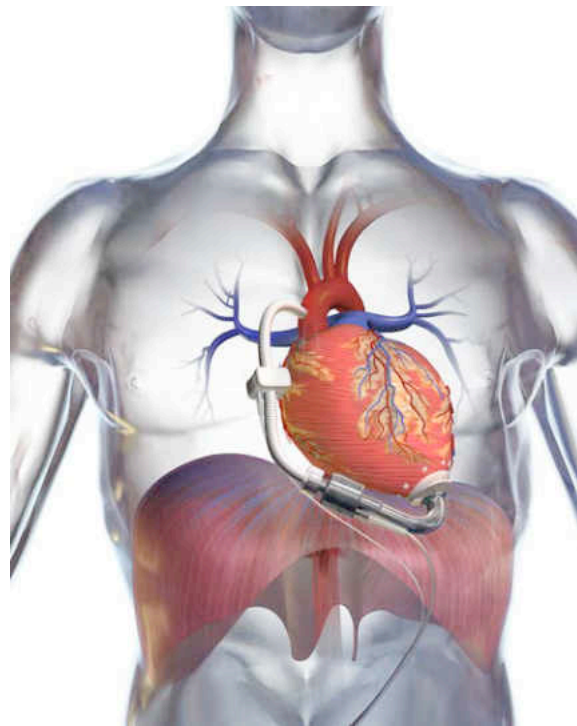
ALE	Arbitrary Lagrangian – Eulerian Formulation
BC	Boundary Conditions
BEM	Boundary Element Method
CFD	Computational Fluid Dynamics
CMM	Coupled Momentum Method
DEM	Discrete Element Model
EF	Ejection Fraction
FSI	Fluid Structure Interactions
HF	Heart Failure
LPM	Lumped Parameter Method
LVAD	Left Ventricular Assist Device
VAD	Ventricular Assist Device

1 CHAPTER 1: INTRODUCTION

Among all possible malfunctions of bodily organs, heart failure, a condition wherein cardiac output cannot satisfy corporal requirement, is the most disconcerting. Dependent upon the condition of the heart, a by-pass is one consideration. In extremis, transplant becomes the best probable solution. Donor compatibility is necessary in order for this procedure to be successful leading to long wait times while seeking donor compatibility and availability. In such cases, a Ventricular Assist Device (VAD) can be implemented as a bridge to transplantation (Figure 1, a-b). Continuous flow pump have shown to be a promising and durable destination therapy. Depending on the workload they almost entirely nullify pulsatile effects, which have been a major cause to thrombo-embolism. In addition VADs been seen to allow room for myocardia recovery. While Ventricular Assist Devices are capable, their efficiency depends upon fluid composition and flow mechanics, and despite improved device design and anti-coagulation treatment, a patient is likely to suffer a thrombo-embolism within a 6 months to a one-year period.



(a)



(b)

Figure 1 - (a) LVAD implantation, (b) LVAD thoracic location.

Incidence of stroke can be reduced significantly by an adjustment of the VAD outflow cannula to direct possible thrombi away from the cerebral vessels towards the other parts of the vasculature where they would cause less harm. Steady flow Computational Fluid Dynamic

(CFD) analyses have indicated reductions of stroke incidence by as much as 50% dependent upon cannula implantation configurations [1,2].

1.1 Vascular Organization

An organism's vasculature serves as a blood flow conduit, carrying oxygen and nutrients to the most basic units of the body, supporting additionally, the immune, reparative and other regulative processes. Despite complexity and scale variation, vasculature can be separated in 5 categories: arteries, arterioles, capillaries, venules and veins (Figure 2).

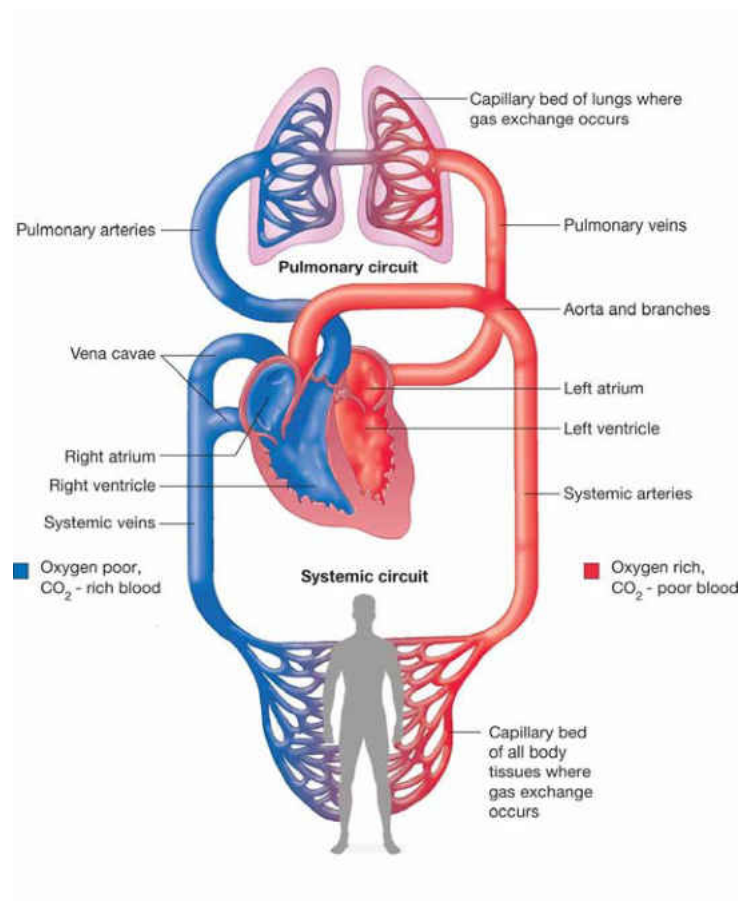


Figure 2 - Circulatory system.

In general, the systems is described as having a fractal structure [3]. In this study, the interest is focused on the arterial system specifically the aortic arch and its outlets to the upper and lower body (Figure 3). Carotid and vertebral arteries supply blood to the head, subclavian arteries carry blood to the arms, coronary arteries feed blood to the heart itself and the descending aorta supplies blood to the lower extremities. Cardiac output (volumetric flow rates) for a typical healthy adult averages at about 5 L/min in a relaxed condition.

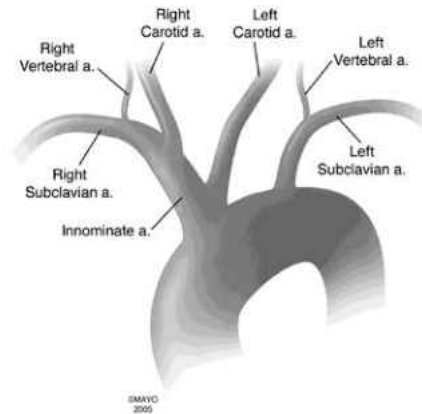


Figure 3 - Aortic arch and branching vessels (Layton, et al. 2006).

A numerical representation of such a variable system (in its entirety) can be quite arduous. Hence, by a method of simplification, vessels are “lumped” into empirically derived representations such as the Windkessel Model to reduce a 3D problem into a 0D version [3,6]. This procedure is referred to as Lumped Parameter Method (LPM). Essentially the Windkessel Model draws an analogy between hydrodynamics (in a 3D scale) and electronics (purely in 0D), providing a simplified method to compute flow properties based on analogous equations and properties in each domain.

Arterial walls follow a 3-layer pattern. The innermost wall (the intima), an intermediate layer (the media) and the adventitia. The intima is mostly composed of endothelial cells, collagen and adhesion cells, and is found to be smooth and non-thrombogenic. The intima represents,

also, the interface where fluid and structure interact. In the media, muscle fibers, which drive the motions of cross-sectional contraction and expansion, are found. The adventitia consists, mainly, of fibroblasts and is believed to act as a containment membrane [3].

1.2 Vascular Diseases

1.2.1 Heart Failure

Heart failure (HF) occurs when the heart is unable to provide sufficient blood flow output to satisfy corporeal requirements. This condition, diagnosed by physical examination, is confirmed by echocardiography. Causes include may include heart attack, hypertension, valvular heart disease and cardiomyopathy. In general, it is possible to quantify heart failure by means of Ejection Fraction (EF), which simply relates the stroke volume (SV) to the end-diastolic volume (EDV) and end-systolic volume (ESV) as in Equation 1.

$$EF(\%) = \frac{SV}{EDV} 100 \quad (1)$$

$$SV = EDV - ESV \quad (2)$$

A typical healthy patient has values ranging from 50 – 70 %. An EF below this range represents a state of cardiomyopathy. An individual's EF tends to decrease gradually due to aging, as the heart's efficiency tends to decrease. However, impaired EF or a sharp inefficiency are consistent indicators of heart failure. A VAD device is usually implemented in this case to support the workload and supply the appropriate amount of blood to regulate bodily functions.

1.2.2 Thrombosis Induced Stroke

Blood clotting, an essential occurrence for homeostasis is a normal process, but vessel deterioration and tissue malfunction can induce undesirable clotting, which may result in stroke, embolism or heart attack. Thrombi generate in two ways: rupture from arteriosclerotic plaques or coagulated masses and fatty deposits dislodged from implanted devices such as VADs (Figure 4).

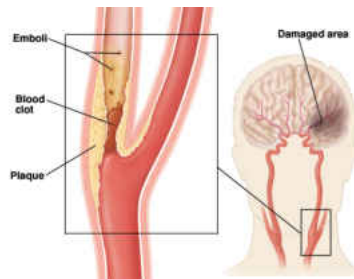


Figure 4 - Blood clots generation by arteriosclerotic plaques and blood clots.

When thrombi obstruct flow in key vessels, either can be fatal. A subject can suffer a stroke in which case cerebral vessels have been occluded or coronary flow is hindered leading to a heart attack. In depth understanding of both cases reveals specific flow patterns in regions of branching, bends, recirculation and low flow. A detailed flow analysis could help optimizing the implementation of VADs to reduce chances of stroke caused by thrombosis.

1.3 Modeling

1.3.1 Patient Specific Geometries

In the past, hemodynamic analysis was carried out on idealized vessel structures whose results were sound, but limited in applications. With the advance of medical imaging techniques such as Magnetic Resonance Imaging (MRI) and Computed Tomography (CT scan) obtaining high resolution volumetric images of the vascular anatomy is now possible [3,4].

These geometries can be used to generate the required meshing to conduct a CFD analysis. Optimized mesh is generated by adaptive methods to reach grid independence and yield greater resolution in the regions of interest (branching and bend) [4].

1.3.2 Boundary Conditions

In early 3D simulations, boundary conditions (BC) were prescribed for the model inlets and outlets in order for the converged solution to match desired conditions. The results, however, deviated from the patient measurements. Modern alternatives are found in MRI that supply in vivo measurements for velocity profiles and pressures [6]. Another option to prescribe BC's is to couple flow rate and pressure in the numerical domain through a 0D model which "lumps" vasculature also known as Lumped Parameter Method [3,4]. By means of adaptive Runge-Kutta solver (RK – 4) the system can be tuned and implicitly solved to provide optimized inlet and outlet conditions to match patient specific measurements. A no-slip condition is applied at the boundary wall to ensure a characteristic viscous flow to ensure a zero velocity profile at lateral walls [3,4].

1.3.3 FSI Coupled with CFD

Traditional research in cardiovascular mechanics employed models, which were idealized, rigid and incompressible. Arterial blood flow in particular has been described by incompressible Navier – Stokes equations in a fixed Eulerian frame of reference and the fluid as Newtonian [3,4,6]. Advances in computational efficiency allow improving inconsistencies by including more realistic flow conditions that account for pressure and velocity variations induced by motions of vascular structures.

This non – rigid structure can be characterized by a Lagrangian frame of reference and is the object of study in the field of Fluid Structure Interaction (FSI). A well-known technique to describe FSI is the Arbitrary Lagrangian – Eulerian formulation (ALE) where the Navier – Stokes equations (Equation 4) of a moving domain are solved with respect to the elastodynamics equations (Equation 5) of the vascular structure which update the computational grid. Kinematic and dynamics compatibility conditions control the process. This method accurately captures interactions between fluid and solid. It can incur time-consuming computations [4], however.

$$\nabla_{\vec{x}} \cdot \vec{v} = 0 \quad (3)$$

$$\rho \frac{\partial \vec{v}}{\partial t} \Big|_{x_o} + \nabla_{\vec{x}} \cdot (\rho \vec{v} \otimes (\vec{v} - \vec{v}_G)) = \nabla_{\vec{x}} \cdot \sigma + \vec{f} \quad (4)$$

$$\rho_o \frac{\partial \vec{v}}{\partial t} + \nabla_o \cdot (\sigma F^{-T}) = \vec{f}_o \quad (5)$$

An alternative to the ALE approach is the Coupled Momentum Method (CMM), which assumes small wall deformation eliminating grid updating. Fluid – structure interaction is enforced by a node – to – node compatibility between the fluid and the wall modeled as a simple membrane. This modification lumps elastodynamic equations and fluid dynamics equation together reducing the degrees of freedom of the problem. CMM is computationally less intensive and retains greater accuracy under the assumption of small deformations [3,4].

1.3.4 Lagrangian Method to Track Microscopic Particulate Flow

Blood is not a monophasic fluid; in fact it presents a complex multiphase combination of cellular elements and plasma – water solution [5]. An interesting case of particulate is the blood clots that can cause stroke. An incompressible fluid whose properties are averages of clinical measurements typically approximates the liquid phase. Physical properties of the cellular

components can undergo changes due to FSI, hence, these microstructures can deform due to flow and flow is affected by the presence of these particles. This duality cannot be overlooked when accurately reproducing a patient's hemodynamics.

A CFD simulation alone is insufficient to model particle – fluid interaction which requires a separate approach. Basic components of thrombi are small enough to be represented by reactive particles whose structures are not important. Such particles can be modeled by the Discrete Element Method (DEM), which disregards fluid – solid interactions [5].

Using this model, thrombogenesis and thrombus transportation can be simulated in the form of mechanical interactions between flow and particles allowing the study of VAD implantations. While running a simulation is then possible tracking particles released in the domain, compute residence time and particle velocities, which can determine the validity of an implant for a patient specific geometry.

1.4 Applications

Combining CFD analysis with FSI to accurately model the fluid domain it is possible to match flow conditions found in patients. Adding DEM allows improving the model further including effect of particulate in blood. Such a realistic model applied to patient specific geometries can have vast medical applications in preventive medicine and surgery [4].

Specifically, in the case of LVAD implants, it is possible to potentially select the most appropriate implementation configuration. Considering that VAD became a destination therapy, device longevity is crucial. Given modern computing power and the numerical model described there is room for device design optimization. In depth study of fluid structure interaction and improvements in numerical computing methods various types of models such as CFD; FSI and

DEM can be implemented in a comprehensive procedure which accurately describe hemodynamics.

In addition, progress in medical imaging techniques such as MRI and CT scan allow performing in – vivo material characterization and in – vivo fluid and solid BC which directly feed data to the numerical model, greatly reducing the error margin.

Predictive medicine through numerical model results promising and far – reaching with plenty of future work to be done to further reduce inconsistencies such as the incompressible flow approximation and the Newtonian – fluid approximation.

2 CHAPTER 2: PROBLEM SET UP

As a whole the problem set-up is meant to be divided in mainly two parts. The LPM section where given some initial conditions, the model solves a system of differential equations producing BC's that then are fed to CFD that in turn solves the problem for the aortic channel in the fluid domain to return both IC and corrected systemic values for the LPM. This loop is required as an intermediate step in order to obtain a fully converged flow field in the aortic model, which can be used for thrombi Lagrangian tracking. Thrombi-embolism predictions can than be carried out by statistical methods over several heart cycles to obtain realistic data.

The conditions under which the model is set to run are for a patient at rest with mild to severe heart failure. Of interest are the flow conditions caused by the LVAD implementation that drastically change flow patterns in the aortic channel. As a consequence thrombi travelling through this section may behave differently. The main point of this research is to capture this phenomenon and establish a predictive model.

At rest the HR in average is of about 65 BPM (beats per minute). To simulate different acuteness of heart failure, a ratio of LVAD-AO (ascending aorta) flow rate in L/min is implemented. A mild-to-severe heart failure can be modeled as the heart provides partial support to the LVAD. A ratio of 4-1 (VAD to aortic outflow) is taken as a representative value of such a case.

Table 1 - Model operational parameters.

Physiological parameter	Value
Heart rate	65 [bpm]
LVAD-AO flow ratio	
Severe HF	4-1 [L min ⁻¹]

2.1 Lumped Parameter Model

The circuit model intends to model the circulatory system based on compliance, flow momentum and vaso-resistance, which give an acceptable approximation. In essence the initial 3-D problem of modeling the total circulation can be reduced to a 50 degree of freedom (DOF) 0-D problem. This model can be advantageous since it can be adapted to any patient specific geometry, given physiological data, free of expenses and can be run several times without any issues. In addition analogies between fluid mechanics and electronics allow manipulating and solving equations to obtain realistic results for comparison.

In fluid mechanics, there are several quantities of interest; the two main ones are usually pressure and mass or volume flow rate, which allow (once obtained) deriving any other relevant result. Pressure in the study of fluid represents a potential that in electronic terms is defined by the voltage, similarly the amount of fluid per unit time, which is caused by a potential, can be represented by the current defined as the amount of charge per unit time.

If we were to observe a simple duct, we would notice that the ducts are able to stretch in both axial and transversal direction, this is generally defined as vaso-compliance. Compliance limits the amount of fluid that a duct can contain. Capacitors in electronics are devices capable of

storing charge, then represent a potential for current flow. Hence when modeling compliance we use a capacitor in the electronic counterpart.

In fluid mechanics, duct geometry and wall friction affects the flow, which in turn controls the pressures in the channel. Similarly resistors affect the flow of charges in a circuit by reducing the potential and obstructing charges, therefore resistors are used to model this physical phenomenon. When a fluid passes through a duct its own inertia prevents it from rapid changes in its momentum, for both magnitude and direction. This particular property of matter can be represented by an inductor which in practice is just a coiled wire, when circulated by a current generates a magnetic field that opposes the flow of current.

Based on the hydraulic analogy it is now possible to design a circuit model, which reproduces the circulatory system. We can combine compliance, resistance and inertia effects altogether using separate components. Keep in mind that in reality all these flow aspects occur simultaneously and not in succession as represented by a circuit.

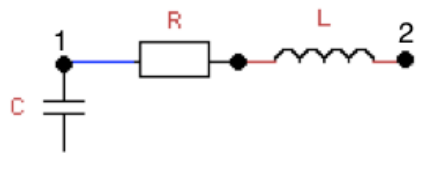


Figure 5 - Basic circulatory circuit element.

Following the Greenfield-Fry approach [1], the entire circulatory system can be modeled starting from one simple schematic shown above in Figure 5. In some cases either capacitors or inductors are omitted in order to simplify the model and reduce computational times, since a tube (for example small veins or capillaries) can be too small to account for compliance and inertia effects can be ignored for small systems (other forces are more influential). It must be noted

however that resistors can never be omitted as it accounts for the geometrical aspects of the model and friction losses, which must be considered at any scale.

As mentioned before the capacitor represents compliance, the inductor inertia and the resistor geometrical induced drag. In the schematic provided above, the set up works in the following manner:

1. At node 1, current comes in if it would be going directly towards node 2 it would encounter resistance hence it charges the capacitor first (generating a voltage/pressure potential);
2. Once the capacitor is fully charged the discharge begins, current flows from node one to node2;
3. At the resistor we have a drop in voltage (pressure);
4. At the inductor the voltage drops once more due to change of current over time;
5. The total change in pressure can be calculated between node 1 and 2. Refer to section 6 for evaluations.

In essence, all the work done by the capacitor is counteracted by the combined efforts of resistor and inductor.

2.2 Circulatory System Model

Starting from the basic circuit model for any vascular vessel, it is now possible to generate the circulatory system in succession following the outlined steps. This is carried out for the left and right heart, pulmonary system, the aortic channel (region of interest), the arterial and venous beds and the cardiac pump. As mentioned earlier, in total this model accounts for a

system of the size a 50 DOF, which mainly focuses on the aortic section of the cardiovascular circulation.

2.2.1 Step 1: Left Heart

The heart in general is composed of 2 atria, 2 ventricles and 2 valves that deliver oxygenated blood to the rest of the upper and lower parts of the organism and receive deoxygenated blood that is supplied to the lungs for re-oxygenation.

Since the heart is a specialized organ, this reflects on its electronic counterpart. To mimic the pumping function of the ventricle (contraction and relaxation), which characterizes a variable compliance, the capacitor in our model has to be time dependent as well. Hence a time variable capacitor is introduced which follows the inverse of an elastance function to reproduce the heart rate (Equation 1). A time dependent component is obtained from curve fitting data as

$$E_n(t_n) = 1.55 \cdot \left[\frac{\left(\frac{t_n}{0.7}\right)^{1.9}}{1 + \left(\frac{t_n}{0.7}\right)^{1.9}} \right] \cdot \left[\frac{1}{1 + \left(\frac{t_n}{1.17}\right)^{21.9}} \right] \quad (6)$$

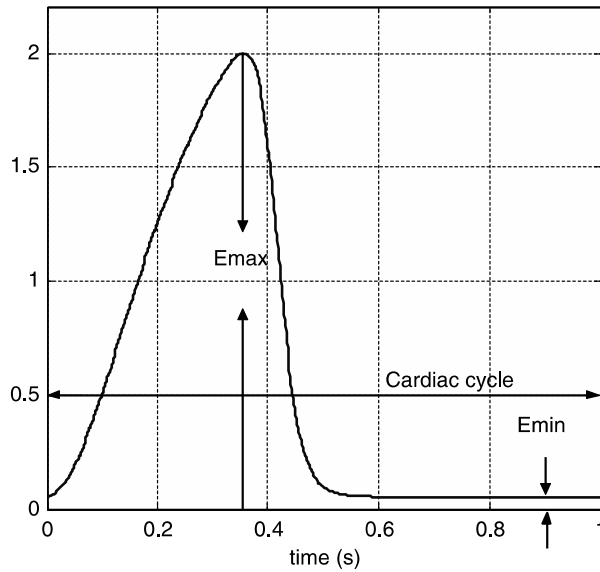


Figure 6 - Elastance function waveform.

This elastance function abides the following relation:

$$E(t) = \frac{LVP(t)}{LVV(t) - V_0} \quad (7)$$

where, $LVP(t)$ stands for left ventricular pressure, $LVV(t)$ left ventricular volume and V_0 is some reference volume at zero ventricular pressure. Referencing to the work by G. Faragallah (et. al), the elastance function that drives the circuit is then obtained by:

$$E(t) = (E_{max} - E_{min}) \cdot E_n(t_n) + E_{min} \quad (8)$$

where, E_{max} and E_{min} are values referring to the end-systolic pressure volume and end-diastolic pressure volume relationships. In physiological observation, it is observed that the heart rate (HR) is tightly related to the cardiac cycle, in fact the in the expression for the elastance in Equation 2, the time variable t_n is defined as:

$$t_n = \frac{t}{T_{max}} \quad (9)$$

Where, t_n is the time normalized by a time constant T_{max} related to the HR as follows:

$$T_{max} = 0.2 + 0.15 \cdot t_c \quad (10)$$

$$t_c = \frac{60}{HR} \quad (11)$$

In addition, to ensure that the flow is unidirectional, two diodes are added in order to model the effective control of the flow by the heart valves.

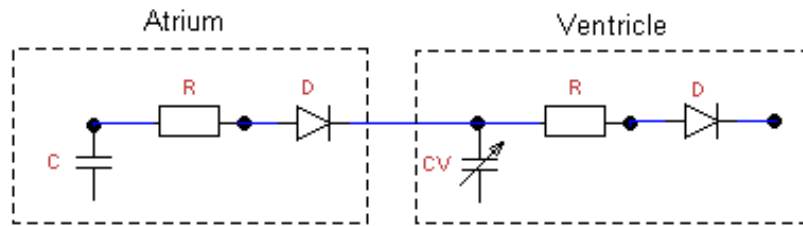


Figure 7 - Heart circuit scheme.

Table 2 - Left heart parameters.

Parameter	Value	Physiological meaning
Resistance [mmHg s mL ⁻¹]		
R _{la}	8.90 10 ⁻⁵	Left atrial resistance
R _{lv}	1.78 10 ⁻⁵	Left ventricular resistance
Compliance [mL mmHg ⁻¹]		
C _{la}	13.33	Left atrial compliance
c _{lv} (t)	Reciprocal of E _{lv} (t)	Left ventricular compliance
Elastance constants		
E _{min} [mmHg mL ⁻¹]	0.049	Diastolic pressure-volume relationship
E _{max} [mmHg mL ⁻¹]	2.49	Systolic pressure-volume relationship
T _{max} [s]	0.338	Normalized time

the particle tracking. In the following table, the resistance values of the tuned model to initiate the iterative process have been listed.

Table 3 - CFD domain resistance parameters [mmHg s mL⁻¹] for 4-1 LVAD-AO flow ratios.

Parameters	4-1 Values	Physiological meaning
R _{ao}	0.1147	Ascending aorta resistance
R _{rc}	1.42	Right coronary resistance
R _{lc}	0.964	Left coronary resistance
R _{ia_cor}	0.0054	Innominate to coronary resistance
R _{can}	0.0677	Cannula resistance
R _{ia_vad}	0.002	Innominate to cannula resistance
R _{ia_rca}	0.0198	Right carotid to innominate resistance
R _{rca}	0.23	Right carotid resistance
R _{ia_rsa}	0.06	Right subclavian to innominate resistance
R _{rsa}	0.176	Right subclavian resistance
R _{rver}	0.939	Right vertebral resistance
R _{lca_ia}	0.00381	Left carotid to innominate resistance
R _{lca}	0.272	Left carotid resistance
R _{lsa_lca}	0.0051	Left subclavian to left carotid resistance
R _{da_lsa}	0.13	Descending aorta to left subclavian resistance
R _{lsa}	0.497	Left subclavian resistance
R _{lver}	1.65	Left vertebral resistance
R _{da}	0.006	Descending aorta resistance

2.2.3 Step 3: Arterial and Venous Beds

Once done with the CFD section, it is necessary to add arterial and venous beds at each outlet. Since the part of interest is the CFD section (in our case the aortic arch), the rest of the system can be simply treated as a stack of arteries, which bring oxygenated blood to the organs, and veins that carry the oxygen-poor blood back to the lungs. This part can then be simplified by two different versions of Figure 5. To model arterial beds, we utilize the complete circuit model. While for veins, since the amount of fluid is greatly reduced, for our purposes inertial effects can be neglected, we omit the inductor. Figure 9 has the circuit schematic.

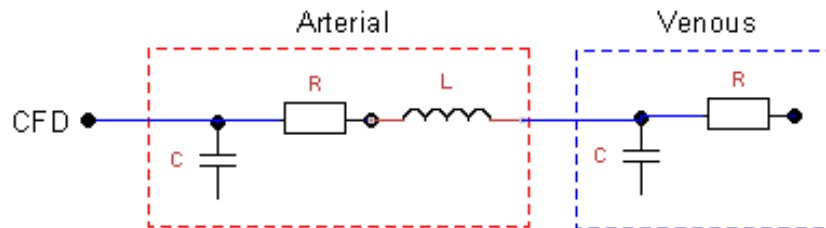


Figure 9 - Arterial and venous beds circuit scheme.

The vascular model can be simplified if desired to reduce the amount of variables to monitor. To achieve this, each outlet maintains its own arterial bed while for paired vessels such as subclavians, carotids, vertebrales and coronaries the venous beds are combined. Each outlet can then be connected to a common node (joint node), which leads to the right heart section, closing the loop. In general this approximates the summation of upper and lower body venous flows that converge to the heart.

Table 4 - Parameters of arterial and venous beds at CFD outlets for 4-1 LVAD-AO flow ratio.

Parameter	4-1 Values	Physiological meaning
R_{rcora}	$R_{rcora}(t)^a$	Right carotid arterial resistance
R_{lcora}	$R_{lcora}(t)^a$	Left carotid arterial resistance
R_{corvb}	12.987	Coronary venous bed resistance
R_{rsb}	3.679	Right subclavian arterial resistance
R_{lsb}	3.679	Left subclavian arterial resistance
R_{dsb}	4.599	Subclavian venous bed resistance
R_{rcb}	3.318	Right carotid arterial resistance
R_{lcb}	3.318	Left carotid arterial resistance
R_{dcb}	4.313	Carotid venous bed resistance
R_{rvb}	10.588	Right vertebral arterial resistance
R_{lvb}	9.86	Left vertebral arterial resistance
$R_{d vb}$	31.233	Vertebral venous bed resistance
R_{da_b}	1.838	Descending aorta resistance
R_{ivb}	4.596	Lower body venous bed resistance
Compliance [mL mmHg ⁻¹]		
C_{rcora}	0.01	Right carotid arterial compliance
C_{lcora}	0.01	Left carotid arterial compliance
C_{corvb}	0.19	Coronary venous bed compliance
C_{rsb}	0.193	Right subclavian arterial compliance
C_{lsb}	0.193	Left subclavian arterial compliance
C_{dsb}	0.097	Subclavian venous bed compliance

Parameter	4-1 Values	Physiological meaning
C_{rcb}	0.193	Right carotid arterial compliance
C_{lcb}	0.2	Left carotid arterial compliance
C_{dcb}	0.1	Carotid venous bed compliance
C_{rvb}	0.029	Right vertebral arterial compliance
C_{lvb}	0.029	Left vertebral arterial compliance
C_{dvb}	0.015	Vertebral venous bed compliance
C_{da_b}	54.3	Descending aorta compliance
C_{ivb}	27.15	Lower body venous bed compliance
Inductor [$\text{mmHg s}^2 \text{mL}^{-1}$]		
L_{rsb}	0.0214	Right subclavian arterial inductance
L_{lsb}	0.0214	Left subclavian arterial inductance
L_{rcb}	0.0214	Right carotid arterial inductance
L_{lcb}	0.0214	Left carotid arterial inductance
L_{rvb}	0.0107	Right vertebral arterial inductance
L_{lvb}	0.0107	Left vertebral arterial inductance
L_{da_b}	0.0005	Descending aorta inductance

^a Refer to Equation 12 for the time dependent coronary arterial resistance function

The coronary arteries represent an exception in the system. From a physiological perspective coronaries are the vessels that carry oxygenated blood to the myocardium. On the other hand vessels that remove the deoxygenated blood from the heart are known as cardiac veins. During systole (contraction) the coronary arteries are compressed due to high ventricular

pressures, which prevents blood flow; most of the perfusion occurs in the diastolic phase (relaxation).

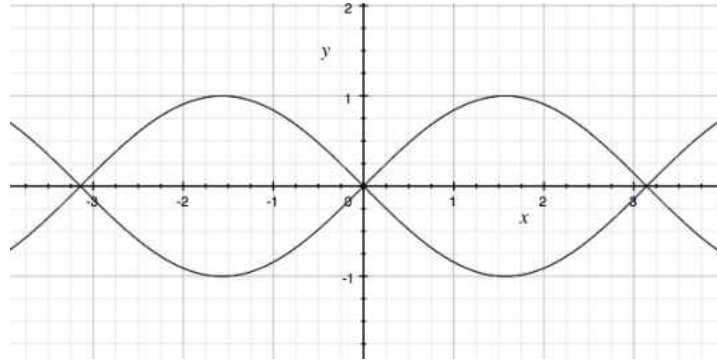


Figure 10 - 180° out of phase waveforms.

Hence to model this phenomenon the coronary circulation has to be out-of-phase as shown in Figure 10. A simple expression based on the elastance function allows us to offset the coronary arterial vascular beds and adjust the magnitude of the waveform:

$$R_{cora}(t) = \left[1.75 \cdot \left(\left| \frac{E_{lv}(t)}{E_{lv}(0)} \right| \right)^2 + 6.796 \right] \cdot R_{fact_cor} \quad (12)$$

where R_{fact_cor} is a scaling factor allows the user to tune the model. The venous bed is then modeled following the venous section of Figure 8. Resistance and compliance are listed in Table 4.

2.2.4 Step 4: Right Heart

The right heart section can be handled in a similar fashion to the left heart, refer to section 2.2.1. Distinctions are made in terms of compliance, resistance and inductance, all dictated by physiological observation. In short, the left heart is due to provide enough pressure to satisfy the required blood supply in the upper and lower body, while the right heart is due to power circulation in the pulmonary system. Hence in magnitude, left heart compliance is greater.

To mimic such an observation, the elastance function expression presented earlier has its E_{\max} and E_{\min} values changed, updated values are found in the following table.

Table 5 - Right heart parameters.

Parameter	Value	Physiological meaning
Resistance [mmHg s mL ⁻¹]		
R_{ra}	$5.94 \cdot 10^{-5}$	Right atrial resistance
R_{rv}	$1.19 \cdot 10^{-5}$	Right ventricular resistance
Compliance [mL mmHg ⁻¹]		
c_{ra}	16.67	Right atrial compliance
$c_{rv}(t)$	Reciprocal of $E_{rv}(t)$	Right ventricular compliance
Elastance constants		
E_{\min} [mmHg mL ⁻¹]	0.0243	Diastolic pressure-volume relationship
E_{\max} [mmHg mL ⁻¹]	0.523	Systolic pressure-volume relationship
T_{\max} [s]	0.338	Normalized time

2.2.5 Step 5: Pulmonary System

Keep in mind that physiologically, the lungs produce very little resistance to the blood flow since they oxygenate the blood. Due to this lungs have also little compliance. Hence when tuning the model one should understand that the parameters for the resistor and the capacitor will be kept smaller than other systemic parameters.

The pulmonary beds are an exception to all others. Physiologically the pulmonary circulatory system is reversed as the pulmonary artery carries hypoxic blood and the pulmonary vein carries oxygen rich blood. Geometrically, these pulmonary veins are larger than any other

veins; therefore inertial effects cannot be entirely neglected. Hence unlike section 3.3 the inductor in the venous bed circuit is not omitted.

Note however that even though inductors in each basic circuit model are considered when it comes to their actual magnitude, they are basically unaccounted for. They only affect the systems in a small part since the values are several orders of magnitude smaller than resistors and capacitors.

2.2.6 Step 6: LVAD

A model for the LVAD was implemented following the work of G. Faragallah (et al.) where the combination of the LVAD pump circuit and the cardiovascular system circuit resulted in a 6th order circuit (Figure 19). In essence, the left heart is modeled in detail, following the CRL scheme. A general compliance, resistance and inductance approximate the aortic channel. A total resistance R_s then represents the rest of the systemic structure, which sums up the resistance offered by the arterial and venous beds. The only variable present in this particular model is the systemic resistance that can be estimated in terms of the LVAD pump flow, based on the observation that at rest the systemic resistance tends to be high and low when active.

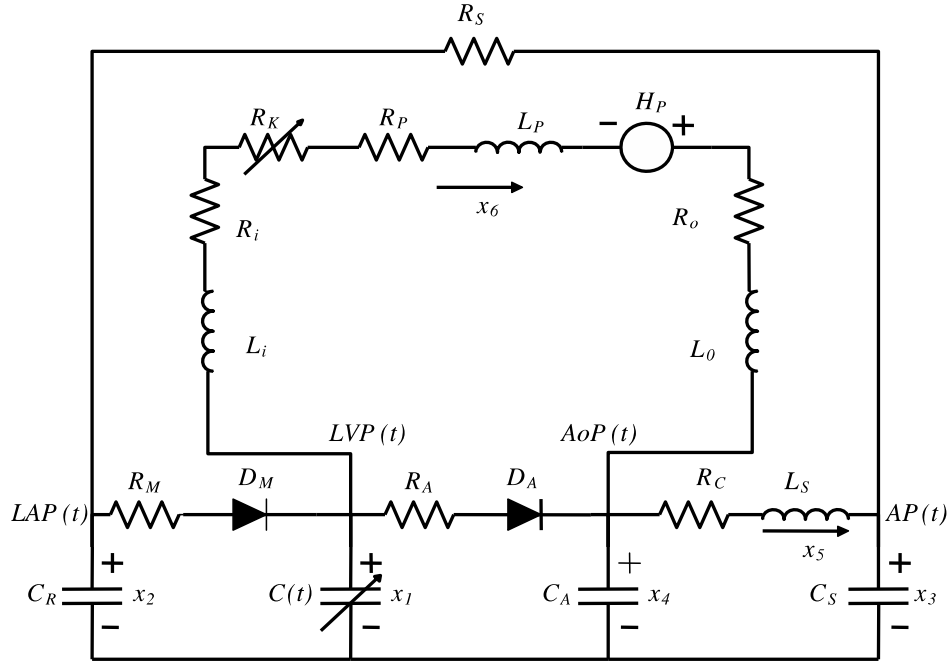


Figure 11 - Closed loop circuit for LVAD implementation, G. Fargallah et. Al [8].

The pump is implemented into the circulatory system in parallel between the left ventricle and the initial node of the aorta as in Figure 11. The drop in pressure across the VAD is expressed by the equation derived by authors as:

$$LVP(t) - AoP(t) = R^*Q + L \frac{dQ}{dt} - \gamma \frac{i(t)}{Q} \quad (13)$$

From this equation, the most important parameter that allows the user to regulate the VAD flow rate is $i(t)$, which represents the amount of current supplied to the pump. Hence by calibrating this unique constant flow conditions between ascending aorta and cannula inlet can be established.

Table 6 - Cardio vascular model parameters in the Faragallah et al. [8] model.

Parameters	Values	Physiological meaning
Resistance [mmHg s mL ⁻¹]		
R _S	1.00	Systemic vascular resistance
R _M	0.005	Mitral valve resistance
R _A	0.001	Aortic valve resistance
R _C	0.0398	Characteristic resistance
Compliance [mL mmHg ⁻¹]		
C(t)	Reciprocal of E _{lv} (t)	Left ventricular compliance
C _R	4.40	Left atrial compliance
C _A	0.08	Aortic compliance
C _S	1.33	Systemic compliance
Inductance [mmHg s ² mL ⁻¹]		
L _S	0.0005	Inertia in blood in aorta

Table 7 - LVAD parameters in the Faragallah et al. [8] model.

Parameters	Value	Physiological meaning
Cannula resistance [mmHg s mL ⁻¹]		
R _i	0.0677	Inlet cannula resistance
R _p	0.1707	Pump resistance
R _o	0.0677	Outlet cannula resistance
Cannula inductance [mmHg s ² mL ⁻¹]		
L _i	0.0127	Inlet cannula inductance
L _p	0.02177	Pump inductance
L _o	0.0127	Outlet cannula inductance

Table 8 - Variable in cardio vascular model.

Variable	Name	Physiological meaning (units)
$x_1(t)$	LVP(t)	Left ventricular pressure [mmHg]
$x_2(t)$	LAP(t)	Left atrial pressure [mmHg]
$x_3(t)$	AP(t)	Arterial pressure [mmHg]
$x_4(t)$	AoP(t)	Aortic pressure [mmHg]
$x_5(t)$	$Q_T(t)$	Total flow [mL s ⁻¹]
$x_6(t)$	$Q_P(t)$	Pump flow [mL s ⁻¹]

In our model, in order to attain the prescribed flow rates found in Table 1 the input current to the VAD was modified. For the 4-1-flow ratio case, this value was set to be 0.03825. Small adjustments are then performed to the global scaling factor to have a matching ventricular waveform with physiological data.

2.2.7 Model Tuning

In order to facilitate the process of tuning the model factors have been implemented to modify parameters such as compliances and resistances in bulk saving the user time. In principle the user must first set capacitance values according to parameters found in literature or through calculations based on physiological data for pressure and flow rates using Equation (24). Once these values have been established inductances can be set to relatively low values initially and finally resistance values can be added in a similar fashion as for capacitance.

By means of the tuning parameters it is now possible to refine the model. Capacitance can be tuned to reach physiological waveforms that lie within a reasonable range as it manipulates vaso-compliance. As the waveforms appear to lie in the same order of magnitude as

a patient's then the model can be finely tuned to replicate the physiological waveforms found in literature. Inductance provides an extra refinement tuning parameter once the model finalized.

2.3 Generating System of Differential Equations

To solve the given circuit, it is necessary to recall the analogy that can be made between electrical concepts and fluid concepts. In the following schematic there are represented all the equations.

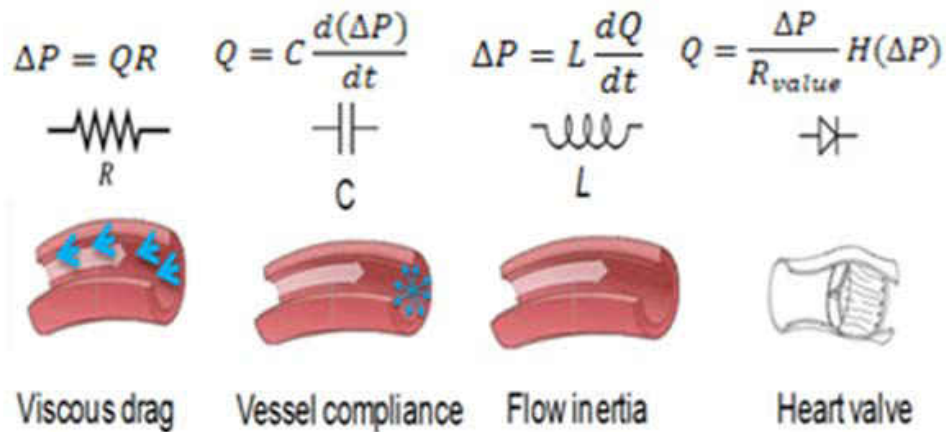


Figure 12 - Hydraulic analogy.

By means of Kirchhoff's node and loop laws which state that the sum of all currents entering and leaving the node has to be equal to zero and that the sum of all voltages in a loop has to be zero as well, it is possible to obtain the required differential equations. Performing this equilibrium equation at every node of the closed circulatory system we obtain a set of differential equations, which can be solved using an adaptive Runge-Kutta, for voltages and currents. These results can then be converted to actual fluid parameters such as pressure and mass/volume flow output.

For consistency in the code, both voltage and current have been labeled a state variable ‘y’. It is important to distinguish the difference between y-voltages and y-currents. In general, every ‘y’ at a node refers to a voltage while every ‘y’ accompanied by an arrows alludes to a current. It can be very helpful when deriving the equations, to couple your work with an extensive schematic in order to keep track.

- Node Law:

1. We can start from the concept stated earlier:

$$\sum I = 0 \quad (14)$$

2. Referring to Figure 8 and Figure 7 (node y_{i+2}) one can perform the current equilibrium at the node as follows.

$$I_{in} + I_C = I_{out} \quad (15)$$

Which can then be written in a more extensive form.

$$y_{i+1} + C \frac{dy_{i+2}}{dt} = \frac{y_{i+2} - y_{i+3}}{R} \quad (16)$$

That can be rewritten in terms of the derivative

$$\dot{y}_{i+2} = \frac{1}{C} (I_{out} - I_{in}) \rightarrow Pressure \quad (17)$$

- Loop Law:

1. In this case the key idea is the following

$$\sum V = 0 \quad (18)$$

2. In general for each elementary circuit loop in Figure 5 the previous expression can be then modified as

$$C_V + R_V + I_V = 0 \quad (19)$$

Or

$$L \frac{dy_{i+1}}{dt} = y_i - Ry_{i+1} - y_{i+2} \quad (20)$$

Now we need to isolate the differential variable

$$\dot{y}_{i+1} = \frac{1}{L}(y_i - Ry_{i+1} - y_{i+2}) \rightarrow Flow \quad (21)$$

Using equations 1 and 2 that were just derived in a general form, modifying the subscripts appropriately one should be able to obtain a system of differential equations that can be solved using a 4th order adaptive Runge-Kutta method.

To avoid any closure problems, at each node in the model, reference voltage are prescribed in order to obtained a closed formed system which can be readily solver by a number of numerical methods. Reference voltage are expressed as follows:

$$V_{ref_i} = y_{\text{voltage before node}} - \left(\sum y_{\text{currents leaving node}} \right) \cdot R_{\text{before node}} \quad (22)$$

In addition to further simplify the system and reduce the algebraic load, expression for the currents are introduced. In Figure 13 there is a full representation of the LPM circuit excluding the LVAD circuit found in section 2.2.6, in the appendix there is an alternative representation that includes the LVAD portion of the circuit. The full set of differential equations can be found in the appendix in the form of a Mathcad spreadsheet snap shots.

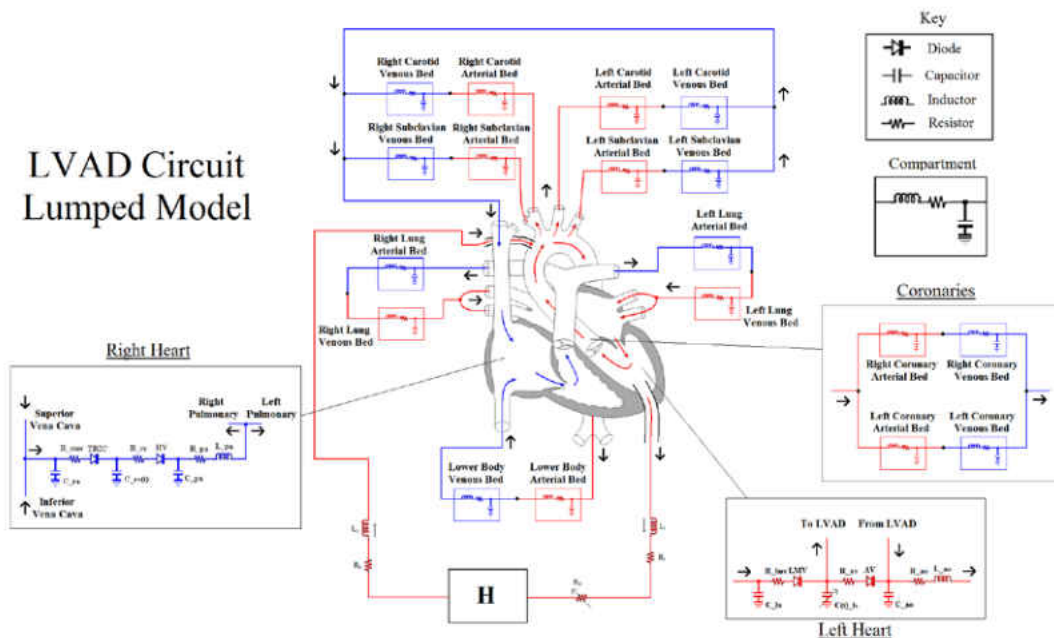


Figure 13 - LVAD circuit LPM.

2.4 Solver

Initially the LPM was designed in Mathcad for simplicity, once the model was validated, it was translated into a much faster version in C++ programming language. In essence, the method implemented to solve the system of ordinary differential equations (ODEs), is an in house adaptive 4th order Runge-Kutta (RK-4). Given a set of initial condition for pressure and flow rates, an absolute error tolerance, an initial number of steps and the system of ODEs, the solver provides an output for however many heart cycle the user requires. This output represents the time-dependent BCs, required in the unsteady CFD model. Reference to the appendix for the full code.

A total of 11 time-varying BCs are generated which provide a waveform that drives the CFD solution to a settled flow field. As a validation procedure, the output waveform for the

ventricular pressure and aortic pressure are sampled in order to compare them to physiological data. In addition, LVAD-AO (ascending aorta) flow rates are monitored to ensure the prescribed flow ratios are maintained.

2.5 CFD Simulation

2.5.1 Fluid Domain

The 3D computation fluid dynamics model is solved using StarCCM++ CFD code. The fluid domain is dictated by a geometry specific aortic channel provided by a patient CT scans (Figure 14), accordingly modified to fit the cannula of the assist device. The mesh was generated using PointWise.

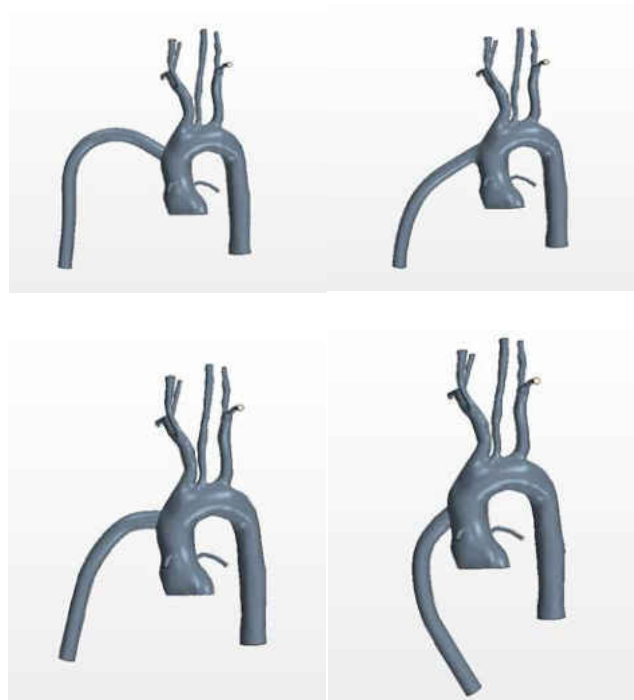


Figure 14 – Patient-specific geometries with LVAD configurations.

The walls of the model are considered rigid to reduce the number of degrees of freedom and simplify the system. However previous work carried out by Osorio et al. [1] in which the same problem was solved for steady state conditions, proved to output realistic solution.

The Eulerian-Lagrangian modeling used has the particles modeled by the Lagrangian scheme and the continuous phase modeled by the Eulerian method. In the simulation blood is modeled as a Newtonian incompressible fluid with density $1060 \frac{Kg}{m^3}$ and dynamic viscosity of $0.004 \frac{Ns}{m^2}$. Transient flow was modeled having $1 \frac{l}{min}$ emanating from the aortic root and $4 \frac{l}{min}$ from the LVAD. As previously mentioned, time-dependent BCs provided by the LPM in terms of pressures and flows are set at 2 inlets and 9 outlets in the form of tabulated files.

Once the BC's are correctly assigned, the model is set up following a necessary scheme based on the required time step and number of inner iterations. Initially to have an initialized flow field based on the BCs, the solver runs for 250 inner iteration. First freezing the time and letting the solver run until the residuals no longer varied determined this. As the initial flow is set, number of inner iterations is decreased to either 200 or lesser iterations, just enough to obtain accurately converged outputs.

The necessary feedback to evaluate the new set of systemic resistances for the aortic channel are obtained by setting cross sectional plane monitors at each location representing a node found in the 0D model.

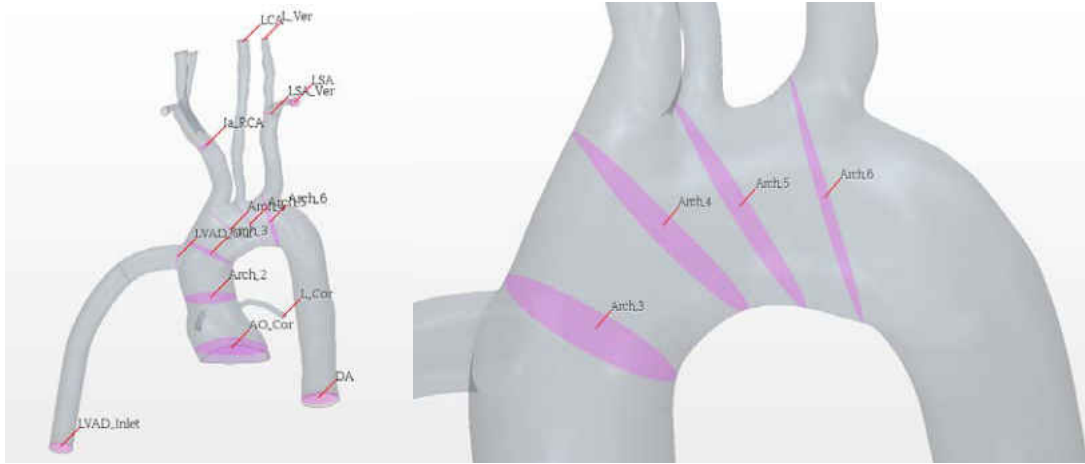


Figure 15 - Monitor cross-section in CFD domain (left) and a close up of the upper aortic arch (right).

The solver is set to run until the physical time is reached. At this point tabulated values for each cross-section are outputted. Once flow and pressure values are collected and time averaged it is possible to calculate resistance by

$$R = \frac{P_i - P_{i+1}}{\dot{m}_i} \quad (23)$$

To evaluate compliance and inductance the following expression can be useful in case it may be necessary to check values measured from the simulation and compare them to the parameters in the LPM.

$$C = \frac{\dot{m}_i \cdot \Delta t}{P_i - P_{i+1}} \quad (24)$$

$$L = \frac{P_i \cdot \Delta t}{\dot{m}_i - \dot{m}_{i+1}} \quad (25)$$

The fluid is modeled to be blood, hence the default properties of water in StarCCM were changed to fit blood specifications.

2.5.2 Particles

The Lagrangian tracking model entails solid spherical non-interacting particles modeled as point masses of set diameter of either 2.5mm or 3.5mm, which are released at the bottom portion of the cannula by an injection grid (Figure 16). The release randomness has been set to have 2 degrees of randomness in time and one degree of spatial randomness.

Spatial randomness is dictated by a point inclusion probability that determines how many nodes in the grid will be injecting a particle at each time step. Randomness in time is introduced by generating a time-dependent particle release table. By means of a random number generating function in Excel with values bounded by 0 and 1 and an imposed time-step about 6 times smaller than the simulation time-step. At a randomized time step, the simulation releases a constant number of particles at random nodes of the grid, one or none per time-step. This ensures realistic statistical variance in the data collected.

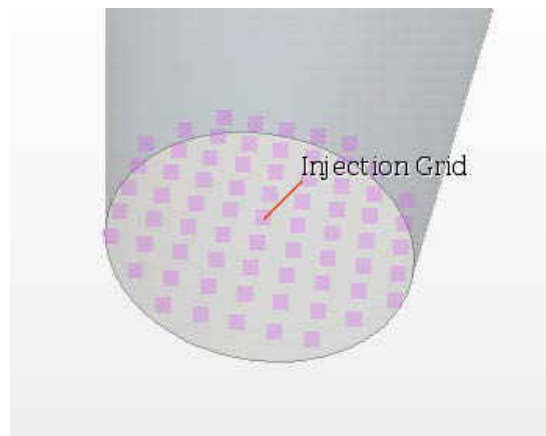


Figure 16 - Injection grid at the base of the inlet cannula.

The specific Excel function used to produce random number was expressed as follows:

$$= \text{randbetween}(0,1) \quad (26)$$

In order to have means of comparison with previous work [1-2] the particulate phase has a constant density of $1116.73 \frac{Kg}{m^3}$ and interactions have been defined in for wall-to-particle interaction as having friction and fully elastic collisions.



Figure 17 - Particle injection at LVAD inlet.

As the model injects particles in the domain (Figure 17), they can be tracked throughout the model using built in track files, which allow the user to count detect particles at different outlets defined by specific boundaries. Simultaneously real-time plots can be generated to quantify the total amount of particles in the domain and the amount of particles leaving or entering the CFD domain at each boundary. These plots can then be tabulated and used for statistical analysis.

2.6 Coupling

As mentioned earlier, before initiating the Lagrangian particle tracking it is imperative for the flow domain to be converged. Hence the LPM and the CFD simulation need to be coupled over several cycles. In addition, to automate the procedure feeding BC's to the

simulation and have the newly evaluated resistances returned to the solver, an intermediate program was added.

The main tasks of this program are to handle the required tables for each iteration and prescribe the number of loops to perform, the number of heart cycles (for both the RK-4 and the CFD), number of steps and number of inner cycles to the RK-4 and CFD solvers.

A schematic of the workflow is provided in Figure 18.

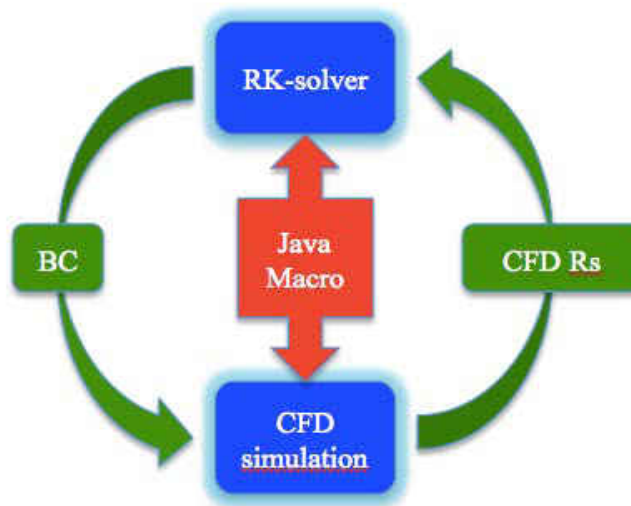


Figure 18 - Coupling loop work flow.

Once the set-up is completed. The entire system is initiated through STAR-CCM+, the Java coupling code is run directly into the simulation, and one iteration is represented by 3 to 5 heart cycles. A certain amount of cycles are run to have converged flow results. Following the user may add however many extra cycles are needed to run particle tracking. A summary of the code is provided, in the appendix.

2.7 Statistical method

In this study the statistical analysis was carried out in two steps: first the body of data relative to thrombus transport was generated to produce means and standard deviations to show consistency throughout runs and compare geometries then the pooled statistics were compared to similar solutions carried out with steady state simulations by means comparison.

Each run produced concise tables of particle transition at every outlet including data recording particle injection into the domain. Particle percentages were then computed with the following expression:

$$Particle\% = \frac{\text{number of particles at outlet}}{\text{number of particles injected}} 100 \quad (27)$$

Once all runs were analyzed, for each particle size and geometry means and standard deviation were evaluated for each outlet and specifically cerebral vessels a statistical method comparing two means was employed to compare steady state simulation and unsteady simulations results to determine whether steady modeling would suffice in order to engage in depth studies on stroke incidence.

The Z-score was calculated based on the probability of a thrombus transitioning through carotid and vertebral arteries in the steady and unsteady cases as:

$$Z = \frac{\mu_1 - \mu_2}{\sqrt{p \cdot q \left(\frac{1}{n_1} - \frac{1}{n_2} \right)}} \quad (28)$$

Where μ_1 and μ_2 represent the means of the two populations, n_1 and n_2 represent the populations sizes, p is the overall probability and $q = 1 - p$. The Z-score is intended to quantify the amount of deviation from a mean based on standard deviations; in a normal distribution 68%

of a populations resides within a standard deviation, 95% of a population resides within two standard deviations and 99.7% of a population resides with three standard deviations. A representation of such a distribution in captured in Figure 19.

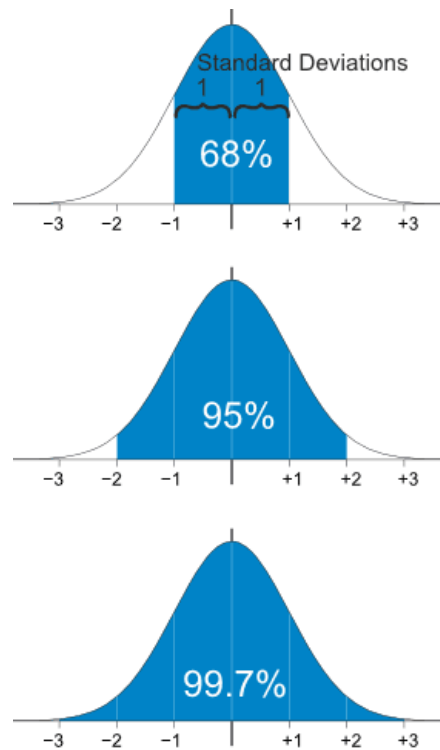


Figure 19 - Normal distribution bell curve.

In this study we employ a two-tailed, two means Z-score, which compares values from two different populations and determines criteria for comparison. A null hypothesis rests on the two populations being very similar, the alternative hypothesis having the two populations being different. A Z-score falling within the confidence interval dictated by standard deviation interval of choice would lead to the rejection of the alternative hypothesis.

3 CHAPTER 3: RESULTS

3.1 LPM Outputs

As aforementioned the LPM models the cardiovascular system and provides BC the CFD code requires to initiate the flow computations. A total of 11 BC are needed to fully define the fluid domain as displayed in the following table.

Table 9 - Definition of BC at each boundary.

Boundary	Definition	Quantity
Ascending Aorta (AO)	Stagnation inlet	Pressure
LVAD	Mass flow inlet	Mass flow
Right Coronary (R_Cor)	Mass flow outlet	
Left Coronary (L_Cor)		
Right Carotid (RCA)		
Left Carotid (LCA)		
Right Subclavian (RSA)		
Left Subclavian (LSA)		
Right Vertebral (R_Vert)		
Left Vertebral L_Vert)		
Descending aorta (DA)		

In order to verify the BCs compare to actual patient measurements waveform at key locations have been produced and compared to values found in literature for mild and acute HF in vivo. This provides this portion of the study with additional validation considering the DOF present in the model.

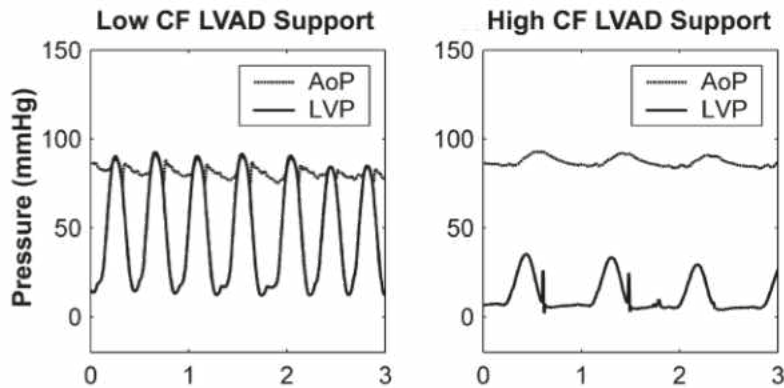


Figure 20 – In vivo pressure waveforms for left ventricle and aorta by Adam R. Travis et. al [11].

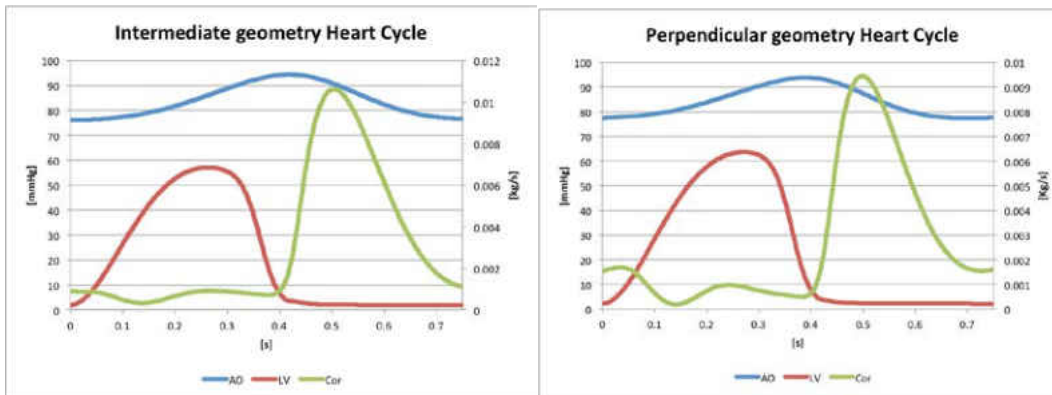


Figure 21 - Pressure and flow rate waveform generated by LPM.

Taking the plot in Figure 20 for high LVAD support and comparing to Figures 21 we see essentially the same wave patterns. A large pressure differential caused by acute heart failure induced by the LVAD maintaining the homeostatic pressure in the aorta. Pressure magnitudes also fit in vivo measurements for both the ventricular pressure and the aortic pressure. Most importantly, physiologically coronaries experience blood flow that is out of phase from the cardiac cycle: flow occurs during the systolic phase. In each case the coronary waveform plotted in Figure 21 displays this trend.

These results validate the LPM we designed as our model closely matches in vivo measurements and realistically maintains physiological flow patterns.

3.2 Flow Field Convergence

For each patient-specific geometry the couple system was ran until a sustained solution was reached. The required iteration may differ based on geometrical and flow features. In the following sections results for the converged solutions will be provided for each case.

In order to test for convergence, for each cross-sectional monitor in the flow domain the tabular values have been averaged and plotted (a sample will be provided for each model for the Ascending Aorta section in Figure 22). Each plot shows the number of iterations required to reach a sustained flow field and provide proof of repeatability.



Figure 22 - AO cross-section monitor plane.

3.2.1 Shift up geometry

With a mesh of about 3 million elements and due to low turbulence at the jet inlet in the aortic channel, this model presented with the fastest iterative rate. One heart cycle can be run in about 6 hours, while 3 heart cycles can take up to a day employing a total of 40 CPUs.

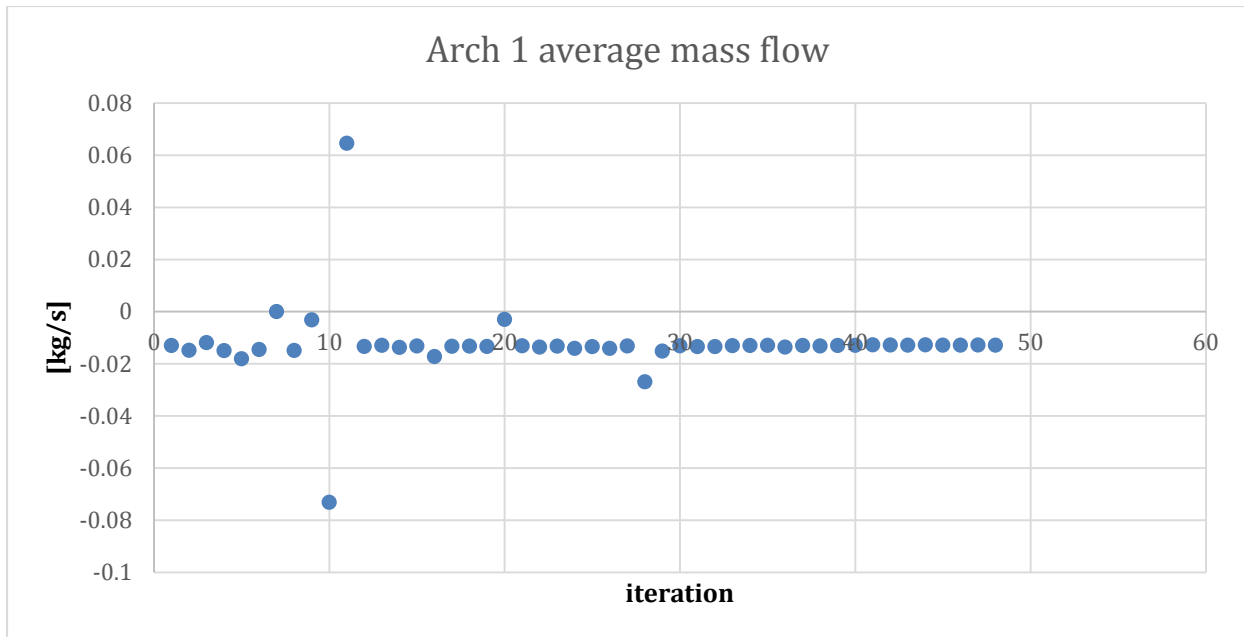


Figure 23 - AO averaged mass flow rate per iteration in shifted-up LVAD.

From the calculations we recognize that at about the 13th iteration the flow field begins to settle to a unique solution. Major spikes in the percent change plot are present due to lack of inner iteration at particular time-steps, which would have required more, causing the solution to deviate. Such deviation were removed by implementing an adaptive iteration criteria that has the model move to the next time step only when residuals for x-momentum, y-momentum, z-momentum, continuity and energy remain steady for several iterations. The plots show the model to be very stable once it reaches the settles flow field, and maintains the same field with negligible variations.

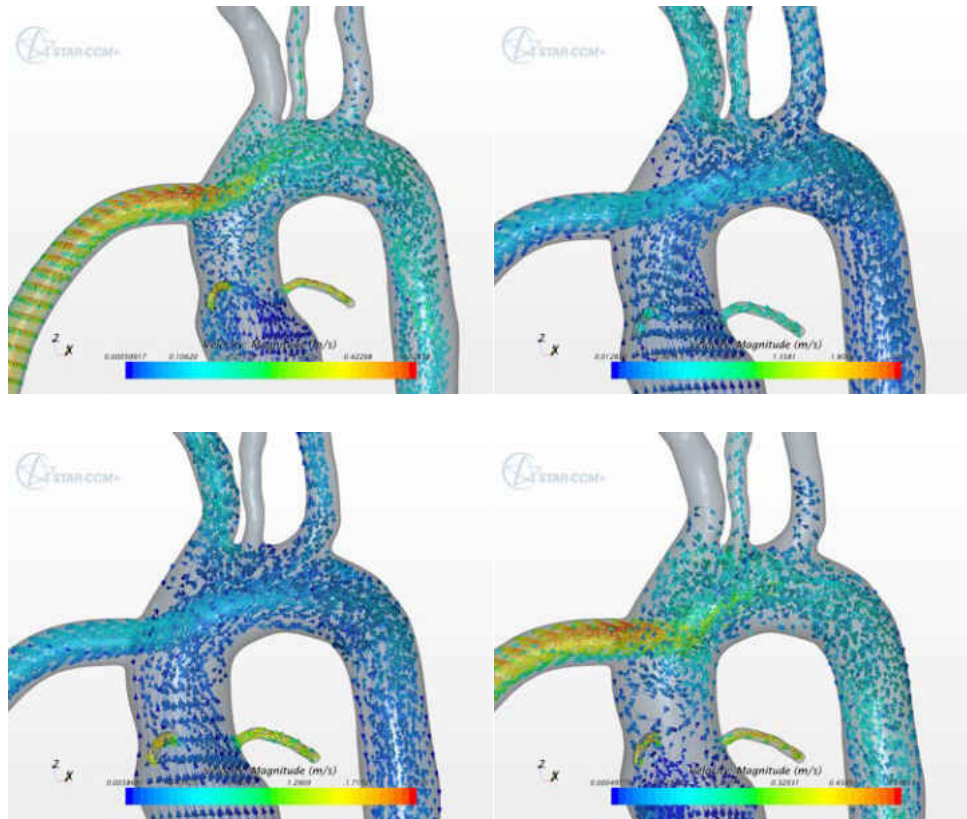


Figure 24 - Streamlines representation through one heart cycle.

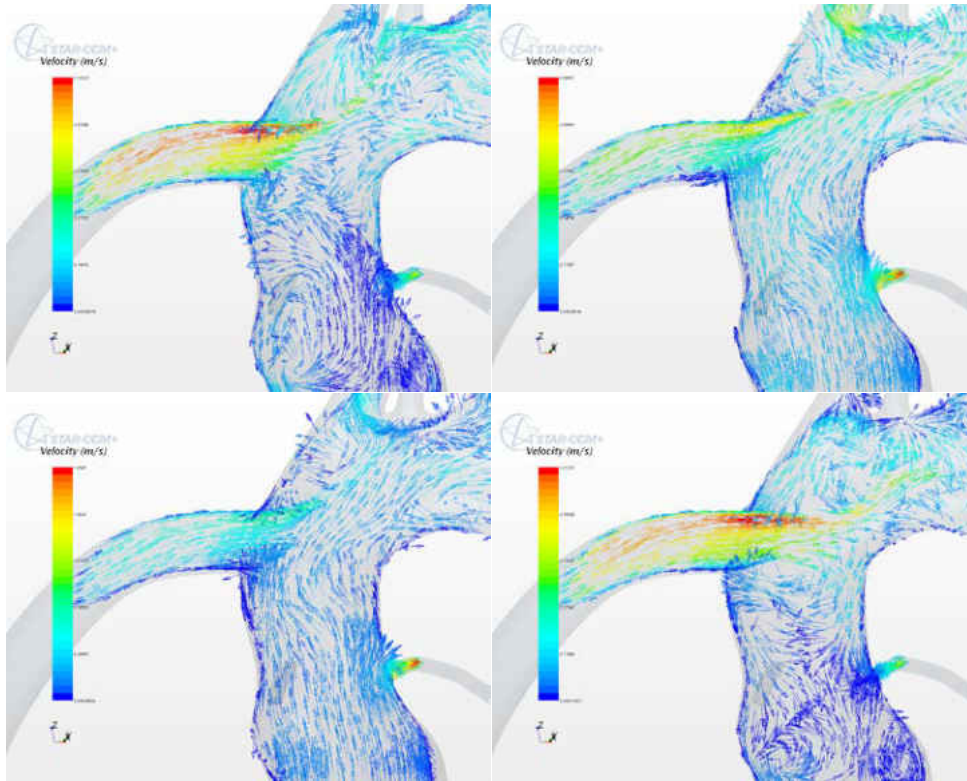


Figure 25 - Vector flow field representation through one cycle.

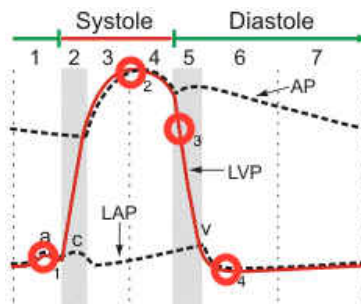


Figure 26 - Cardiac cycle.

Figures 24-25 show flow field representation at key locations through the heart cycle, in systole and diastole for a sustained solution. Jet interaction with flow emitted from the aortic root are clearly modeled and represented. The cannula jet experiences slight impingement on the opposing interior aortic wall. Through a cardiac cycle the jet suffers minor fluctuations due to the interaction with the cardiac ejected flow. This phenomenon is to be expected given the pulsatile

nature of the flow. At the peak of the cycle this interaction also produces large areas of recirculation at the base of the innominate artery, which could potentially cause particles to stagnate and embolize to the cerebral vessels. A much smaller degree of recirculation is generated by the weak impingement in the aortic root. This could similarly cause embolization in the eventuality of a particle transitioning in the region. It is noted that we can observe the out-of-phase flow present in the coronary vascular bed.

3.2.2 Perpendicular geometry

In this case the grid converged mesh present about between 1-2 million cells, and an increased number of cells in the jet inlet was required due to high recirculation as the jet impinges onto the facing aortic wall. One heart cycle can be run in 12 hours and 3 cycles require about 2 days and a half when using 60 CPUs. Considering the turbulent phenomena the simulation proved to be fast-paced.

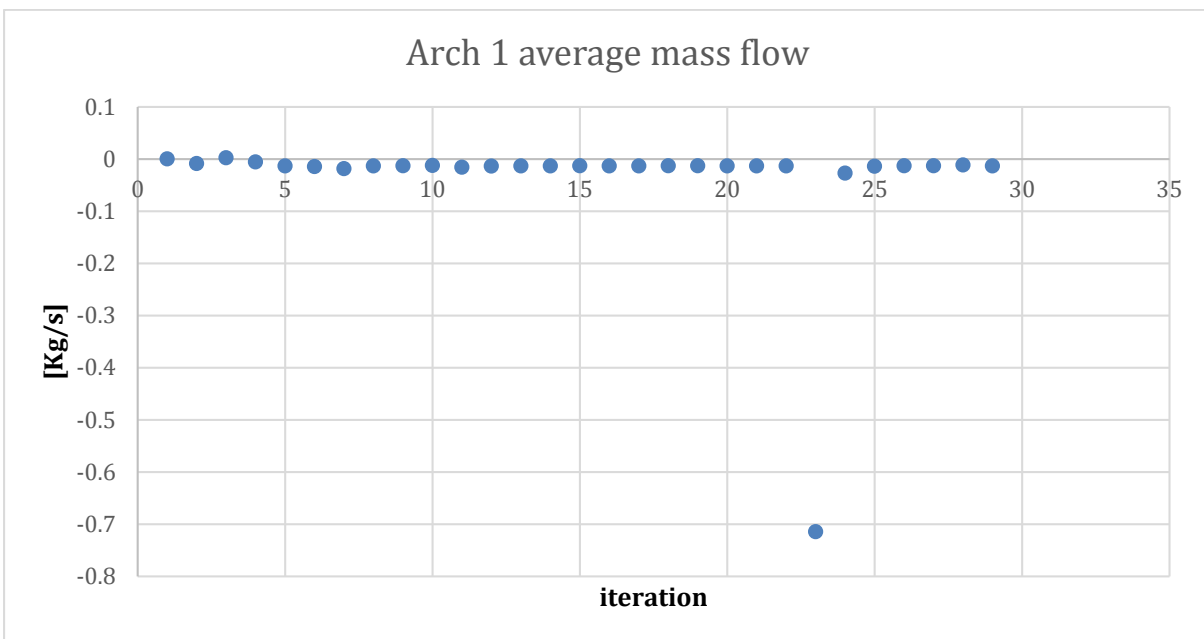


Figure 27 - AO averaged mass flow rate per iteration in perpendicular LVAD.

Based on the above computations we recognize that at about the 15th iteration the flow field begins to settle to a unique solution. Once again major deviations are due to lack of inner iteration at particular time-steps, which would have required more, causing the solution to deviate. But the loop shows to converge fast right after. Just as for the shift-up geometry the perpendicular model demonstrates stability for the settled solution.

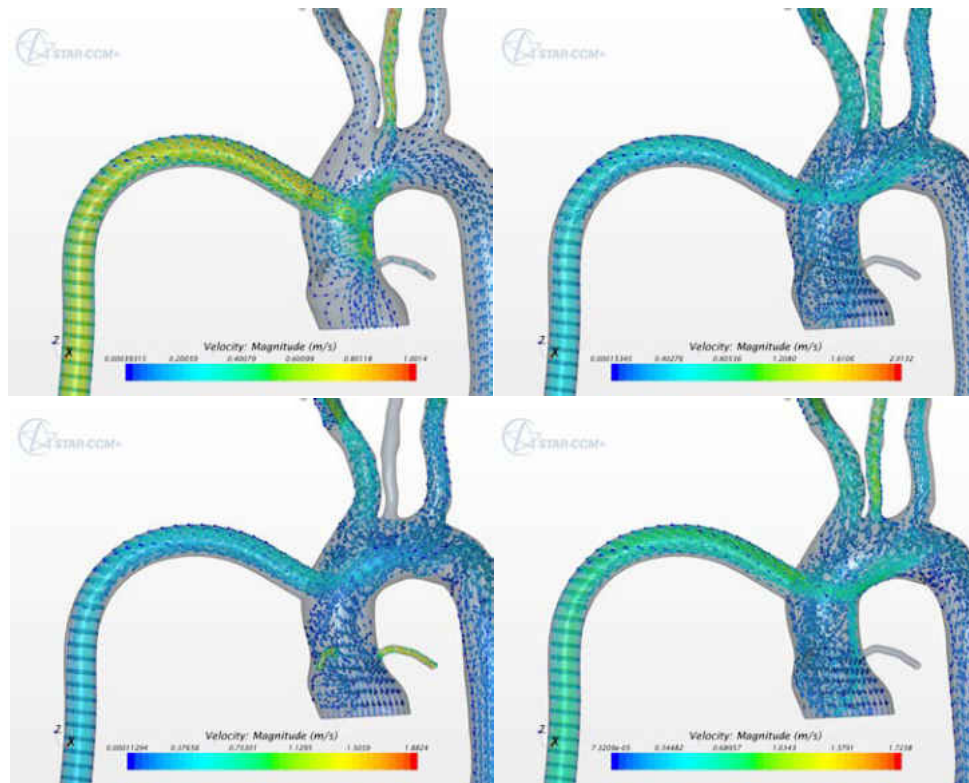


Figure 28 - Streamlines representation through one heart cycle.

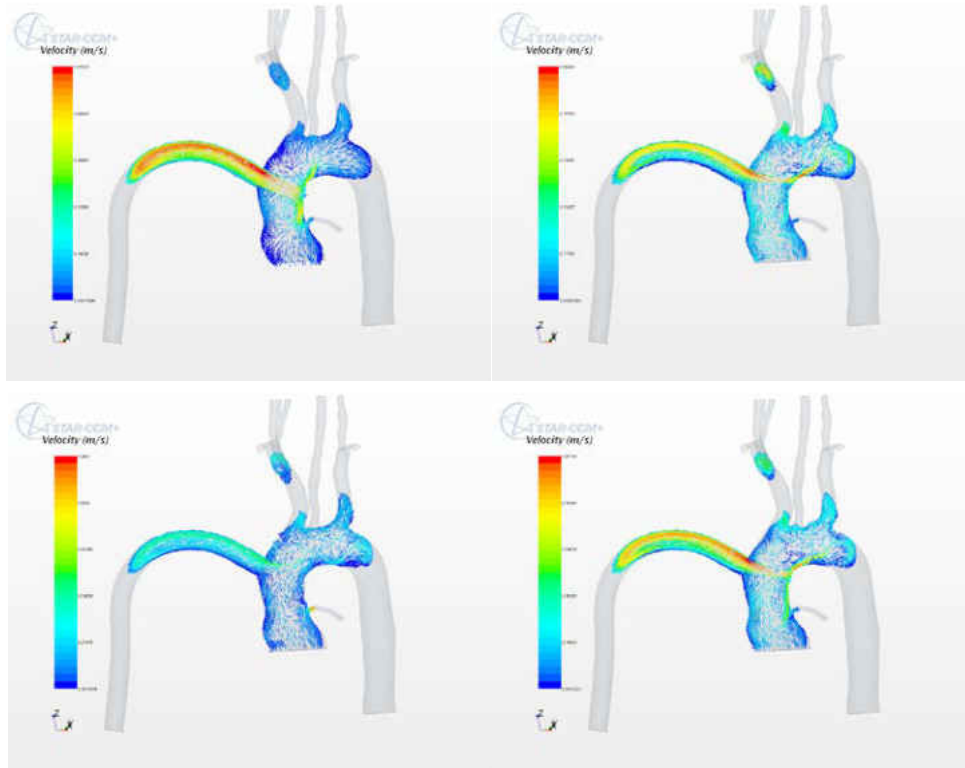


Figure 29 - Vector flow field representation through one heart cycle.

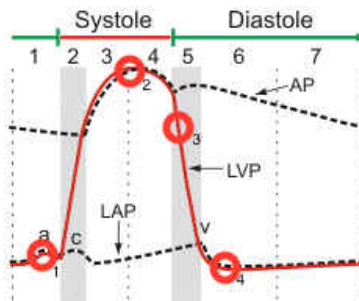


Figure 30 - Cardiac cycle.

As for the intermediate geometry, Figures 26-27 show a sustained flow field solution at key locations through the heart cycle, in systole and diastole. Jet interaction with flow emitted from the aortic root are clearly modeled and represented. Jet impingement is effectively represented in both visualizations. The strong impingement causes stagnant flow and major recirculation due to large losses in momentum in the continuous phase. Close inspection shows

that we find strong recirculation in the aortic root near the coronary arteries and in the upper portion of the aortic arch. This phenomenon can cause thrombi to experience increased residence period in sensitive areas at risk of occluding cerebral and cardiac vessels increasing potential morbidity due to the VAD implantation. In addition the aforementioned interaction causes cannula jet oscillations, which strongly indicate periodic flow patterns not captured in a steady state model. Again we can observe the out of phase flow present in the coronary vascular bed.

4 CHAPTER 4: DISCUSSION OF PARTICLE TRACKING RESULTS

Various percentages for particles entering vertebral and carotid vessels are displayed in Table 9. In all cases thrombo-embolization tends to mainly occur in the carotid arteries. A more detailed summary of all collected data can be found in the Appendix C for each vessel and geometry.

Table 10 - Percentages of particle entering cerebral vessels.

Configuration	Particle size								
	Vertebrals		Carotids		Overall		Overall		
	2.5mm	3.5mm	2.5mm	3.5mm	2.5mm	3.5mm	Vertebrals	Carotids	Total
Intermediate	3.59±1.52	3.53±1.33	24.98±1.44	25.70±3.19	28.57±1.27	29.23±4.48	3.87±0.57	25.99±1.89	28.81±2.03
Perpendicular	0.94±0.92	0.78±0.70	8.22±1.53	10.93±2.97	9.16±0.69	11.71±3.02	0.95±0.64	8.99±1.17	10.33±1.33

Embolization rates for cerebral vessels involving particles of size 2.5mm result significantly higher for the intermediate geometry in both vertebral and carotid arteries. This translates in increased stroke chances directly caused by this specific diameter. A similar fashion is observed for particles of 3.5mm diameter.

Furthermore there seems to be a correlation between stroke rate probability and particle size. As particle size increases the embolization rate tend to rise as well. In the carotid vessels this occurs more markedly than in vertebral arteries. As aforementioned, the statistical comparison of means is obtained imposing a 95% confidence interval, and incurring in the null hypothesis when having equal means. The alternative hypothesis yields different means.

Table 11 - Testing criteria for null hypothesis $\mu_1 - \mu_2 = 0$.

Alternative hypothesis	Reject null hypothesis if:
$\mu_1 - \mu_2 \neq 0$	$Z > 1.96$ or $Z < -1.96$

A Z-score between 1.96 and -1.96 would translate into the rejection of the alternate hypothesis and Z-score of 0 would prove equal means.

Table 12 - Z-score of mean comparison between steady and transient models.

		Particle size					
		Overall					
configuration	Mode	2.5	3.5		Vertebrals	Carotids	total
Intermediate	Unsteady	28.57±1.27	29.23±4.48		3.87±0.57	25.99±1.89	28.81±2.03
	Steady ^a	18.44±0.76	11.11±1.19	11.15±2.36	1.39±1.18	12.17±1.42	13.56±1.59
Z-score		10.76	23.43	23.35	12.09	24.43	25.76
Perpendicular	Unsteady	9.16±0.69	11.71±3.02		0.95±0.64	8.99±1.17	10.33±1.33
	Steady ^a	21.38±1.71	10.97±1.27	9.31±1.02	1.75±1.33	12.13±0.91	13.89±1.36
Z-score		-7.69	0.46	1.59	-1.97	-3.10	-3.31

^a Statistical data, means and standard deviation excerpted from Kassab et al. 2014[9].

In Table 12 the comparison of the transient solution to the steady state solution through the evaluation of the two population Z-score. For the intermediate geometry simulation releasing 2.5mm particles we see that the means for the total amount of particles traveling to the cerebral vessels turn out to not to be comparable has the null hypothesis is rejected. This is mainly due to the fact that the interaction between the cannula jet and the aortic root flow do not behave similarly in either mode. For the transient case the jet experiences oscillations caused by the periodic aortic root flow, hence particles will not travel following similar patterns since pulsatility has been introduced.

The perpendicular geometry on the other hand presents strong cannula jet impingement, which causes stagnation in the region. Due to the pulsatile nature of the flow entering from the aortic root, the jet tends to undergo marked fluctuations that can be clearly shown by the moving stagnation point on the aortic wall facing the cannula (Figure 26). These jet oscillations change

the flow pattern of the continuous phase but more importantly drastically affect particle transition in the region. Due to the smaller size of the particles, cloths appear to be more responsive to flow pattern changes. This phenomenon is reflected in the rejection of the null hypothesis.

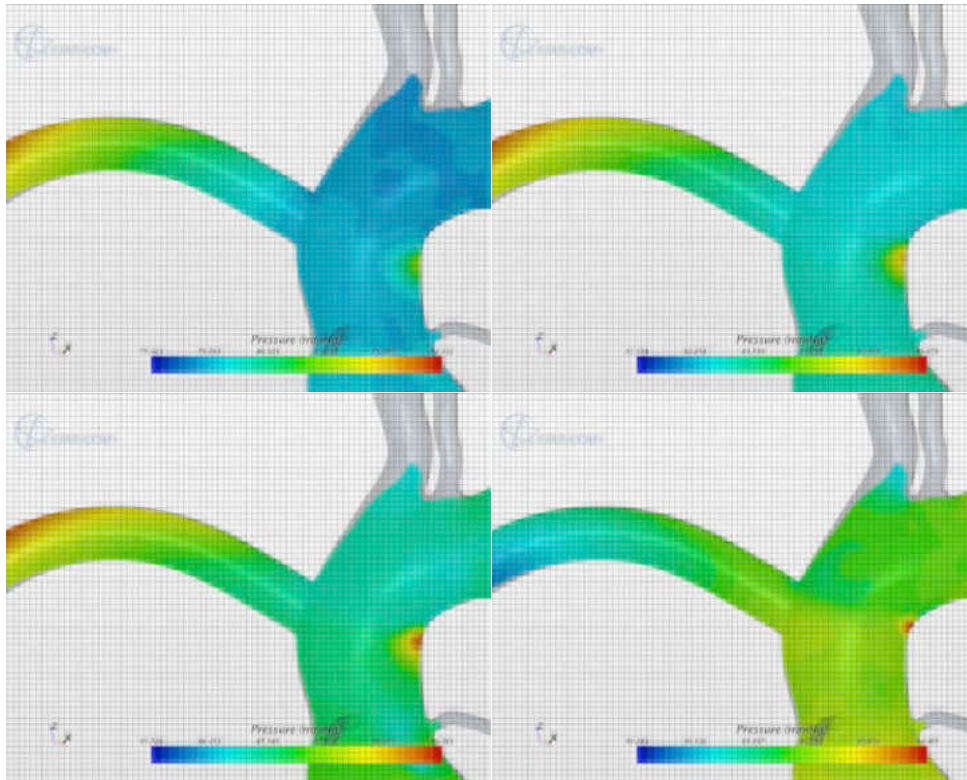


Figure 31 - Stagnation point migration through systolic phase.

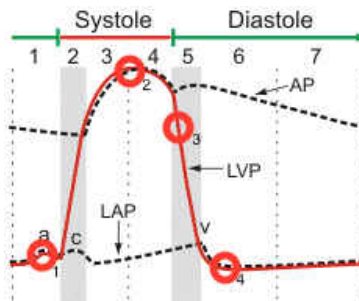


Figure 32 - Cardiac cycle.

When releasing 3.5mm particles implementing an intermediate VAD suture means do not compare. In fact the means for the transient model show an opposite, increasing trend to the

steady state case. This is dictated by a similar phenomenon to the oscillating jet in the case of the perpendicular geometry. To a small degree the cannula jet suffers a pulsatile push-and pull from the aortic root, which coupled to the increased particle, size results in increased stroke chances as the particles get pushed into the cerebral vessels.

In a perpendicular geometry the mean for stroke induced by 3.5mm particle compares to the steady state case. Again the oscillating jet phenomenon is strongly present; the increased particle size causes cloths to be increasingly affected by the flow field. Due to the large amount of momentum loss induced by the constant jet impingement, particles for the steady case and the transient case behave in much the same way. A Z-score rejecting the alternate hypothesis supports this observation.

The aim of this study is to quantify stroke rate for a transient model scheme and compare the results to a similar experiment carried out under steady state conditions. This study however brings to light another phenomenon, which could be of particular interest and deserves a great deal of attention.

Table 13 - 3.5mm particle data for Ascending Aorta in the perpendicular geometry.

run	%
1	23.53
2	13.33
3	29.37
4	34.36
5	26.18
mean	25.35
st dev	7.01
variance	25.35±7.01

As shown in Table 13 for a perpendicular cannula configuration there is a significant amount of particles recirculating in the ascending aorta region as a result of strong jet impingement. This raises concerns as such particles can potentially occlude the coronary arteries at the root of the aortic arch causing a heart attack. Further investigation may reveal additional techniques that could mitigate the strong vorticity and recirculation observed.

5 CHAPTER 5

5.1 Conclusion

It was established clearly from the steady state CFD computations it was clear that VAD cannula angle orientation configuration can greatly affect the fraction of thrombi originating from the VAD embolizing in the cerebral vessels [9]. Proper adjustment of the cannula implantation can potentially reduce stroke risk. The introduction of pulsatile flow shows, however, a change in the predictions brought forth by the steady state models. Cannula jet oscillations cannot be neglected as they dramatically change the flow field transporting the particles. In addition to stroke risk computations this study brings forth the possibility of further investigation in likely event of occlusion in vessels supplying blood to the cardiac muscles that may lead to heart attack which is an equally fatal occurrence.

Hence we have additional insight on acceptable simplifications and required specifications that a predictive model would need in order to be reliable for medical applications. Depending on particle size and angle implementation, a steady state study may be sufficient while for other cases pulsatile flow is necessary to accurately depict flow pattern and embolization rates.

5.2 Future Work

The results provided by this procedure deemed to be quite realistic and provide a good approximation thrombo-embolization through particle tracking. As mentioned before, a particularity of this work was dictated by the lack of particle-to-particle interaction, which might reduce the degree of accuracy. However to reduce computational periods, this approximation was deemed necessary and appropriate. The next step to be taken is to consider partially elastic

wall-to-particle and particle-to-particle interactions dictated by restitution coefficients. This addition will ensure greater accuracy in the model.

A further step will be to add fluid-to-structure interaction (FSI) that marks the transition between a rigid aortic model, to a compliant one. Such a degree of complexity will definitely set a new standard for circulatory modeling in the bioengineering field. In addition as a further method of validation, our group is currently working on a bench top model with compliant arterial and venous beds, which would closely match the simulated model discussed in this project. In order to implement compliance, Windkessels structures are included. The aortic artery will still be modeled having rigid walls; however adding bed compliance represents a definite step forward from previous work [1]. A pulsatile pump will generate a waveform and a continuous flow pump will simulate the LVAD.

APPENDIX A: EQUATIONS

(29) LPM ODEs $D(y,t)=f$

In the following pages find the expression for the right hand side of equation 15.

$$\begin{aligned}
& \frac{1}{c_{ap}}(i_{10}(y) - y_2) \\
& \frac{1}{L_{ap}}(y_1 - y_2 \cdot R_{ap} - y_5) \\
& \frac{1}{c_{vp}}(y_2 - y_4) \\
& \frac{1}{L_{vp}}(y_3 - y_4 \cdot R_{vp} - y_5) \\
& \frac{1}{c_{la}}(y_4 - i_2(y)) \\
& \frac{1}{c_{lv}(t)}(i_2(y) - i_3(y) - y_6 \cdot dc_{lv}(t) - y_7) \\
\text{VAD_Condition} \cdot \frac{1}{L_{star}} \left(y_6 - y_{29} - R_{star}(y_6, x1) \cdot y_7 + \gamma \cdot \frac{i_{vad}}{y_7} \right) \\
& \frac{1}{c_{ao}}(i_3(y) - y_9) \\
& \frac{1}{L_{ao}}(y_8 - y_9 \cdot R_{ao} - V_cfd_1(y)) \\
& \frac{1}{L_{cr}}(V_cfd_1(y) - y_{10} \cdot R_{cr} - y_{27}) \\
& \frac{1}{L_{cl}}(V_cfd_1(y) - y_{11} \cdot R_{cl} - y_{28}) \\
& \frac{1}{L_{ia_cor}}(V_cfd_1(y) - y_{12} \cdot R_{ia_cor} - V_cfd_2(y)) \\
\text{VAD_Condition} \cdot \frac{1}{L_{cannula}}(y_{29} - y_{13} \cdot R_{cannula} - V_cfd_2(y)) \\
& \frac{1}{L_{ia_vad}}(V_cfd_2(y) - y_{14} \cdot R_{ia_vad} - V_cfd_3(y)) \\
& \frac{1}{L_{rca_ia}}(V_cfd_3(y) - y_{15} \cdot R_{cl} - V_cfd_4(y)) \\
& \frac{1}{L_{rca}}(V_cfd_4(y) - y_{16} \cdot R_{rca} - y_{30}) \\
& \frac{1}{L_{ia_rsa}}(V_cfd_4(y) - y_{17} \cdot R_{ia_rsa} - V_cfd_5(y))
\end{aligned}$$

$$\begin{aligned}
& \frac{1}{L_{r_ver}} \cdot (V_cfd_5(y) - y_{18} \cdot R_{r_ver} - y_{31}) \\
& \frac{1}{L_{rsa}} \cdot (V_cfd_5(y) - y_{19} \cdot R_{rsa} - y_{32}) \\
& \frac{1}{L_{lca_ia}} \cdot (V_cfd_3(y) - y_{20} \cdot R_{lca_ia} - V_cfd_6(y)) \\
& \frac{1}{L_{lca}} \cdot (V_cfd_6(y) - y_{21} \cdot R_{lca} - y_{33}) \\
& \frac{1}{L_{lsa_lca}} \cdot (V_cfd_6(y) - y_{22} \cdot R_{lsa_lca} - V_cfd_7(y)) \\
& \frac{1}{L_{da_lsa}} \cdot (V_cfd_7(y) - y_{23} \cdot R_{da_lsa} - V_cfd_8(y)) \\
& \frac{1}{L_{l_ver}} \cdot (V_cfd_8(y) - y_{24} \cdot R_{l_ver} - y_{34}) \\
& \frac{1}{L_{lsa}} \cdot (V_cfd_8(y) - y_{25} \cdot R_{lsa} - y_{35}) \\
& \frac{1}{L_{da}} \cdot (V_cfd_7(y) - y_{26} \cdot R_{da} - y_{36}) \\
& \frac{1}{c_{rcorab}} \cdot \left[y_{10} - \left(\frac{y_{27} - y_{37}}{R_{rcora}(t)} \right) \right] \\
& \frac{1}{c_{lcorab}} \cdot \left(y_{11} - \frac{y_{28} - y_{37}}{R_{lcora}(t)} \right) \\
& \frac{1}{c_{cannula}} \cdot (y_7 - y_{13}) \\
& \frac{1}{c_{rcb}} \cdot (y_{16} - y_{41}) \\
& \frac{1}{c_{rvb}} \cdot (y_{18} - y_{44}) \\
& \frac{1}{c_{rsb}} \cdot (y_{19} - y_{38}) \\
& \frac{1}{c_{lcb}} \cdot (y_{21} - y_{42}) \\
& \frac{1}{c_{lvb}} \cdot (y_{24} - y_{45})
\end{aligned}$$

$$\begin{aligned}
& \frac{1}{c_{lsb}} \cdot (y_{25} - y_{39}) \\
& \frac{1}{c_{da_b}} \cdot (y_{26} - y_{47}) \\
\frac{1}{c_{corvb}} & \cdot \left[\left[\left(\frac{y_{27} - y_{37}}{R_{rcora}(t)} \right) + \left(\frac{y_{28} - y_{37}}{R_{lcora}(t)} \right) \right] - \left(\frac{y_{37} - y_{49}}{R_{corvb}} \right) \right] \\
& \frac{1}{L_{rsb}} \cdot (y_{32} - y_{38} \cdot R_{rsb} - y_{40}) \\
& \frac{1}{L_{lsb}} \cdot (y_{35} - y_{39} \cdot R_{lsb} - y_{40}) \\
& \frac{1}{c_{dsb}} \cdot (y_{38} + y_{39} - i_5(y)) \\
& \frac{1}{L_{rcb}} \cdot (y_{30} - y_{41} \cdot R_{rcb} - y_{43}) \\
& \frac{1}{L_{lcb}} \cdot (y_{33} - y_{42} \cdot R_{lcb} - y_{43}) \\
& \frac{1}{c_{dcb}} \cdot (y_{41} + y_{42} - i_6(y)) \\
& \frac{1}{L_{rvb}} \cdot (y_{31} - y_{44} \cdot R_{rvb} - y_{46}) \\
& \frac{1}{L_{lvb}} \cdot (y_{34} - y_{45} \cdot R_{lvb} - y_{46}) \\
& \frac{1}{c_{dvb}} \cdot (y_{44} + y_{45} - i_7(y)) \\
& \frac{1}{L_{da_b}} \cdot (y_{36} - y_{47} \cdot R_{da_b} - y_{48}) \\
& \frac{1}{c_{ivb}} \cdot (y_{47} - i_8(y)) \\
& \frac{1}{c_{ra}} \cdot (I_{in}(y) - i_9(y)) \\
& \frac{1}{c_{rv}(t)} \cdot (i_9(y) - i_{10}(y) - y_{50} \cdot dc_{rv}(t))
\end{aligned}$$

(30) Auxiliary current and reference voltage equations

-----Current coming in to the Right Heart-----

$$I_{in}(y) := i_5(y) + i_6(y) + i_7(y) + i_8(y) + i_{11}(y)$$

Reference Voltage for Pulmonary Intro

Output LVAD Voltage

$$v1(y) := \frac{i_7(y) + \left(\frac{y_1}{R_{rpa}} + \frac{y_3}{R_{lpa}} \right)}{\frac{1}{R_{rpa}} + \frac{1}{R_{lpa}}}$$

$$V_{vad}(y) := y_7 \cdot R_{star}(y_6, x1) + y_6$$

Reference Voltges for Inside CFD

$$V_{cfd_1}(y) := y_8 - (y_{10} + y_{11} + y_{12}) \cdot R_{ao}$$

$$V_{cfd_2}(y) := V_{cfd_1}(y) - (y_{14} - y_{13}) \cdot R_{ia_cor}$$

$$V_{cfd_3}(y) := V_{cfd_2}(y) - (y_{15} + y_{20}) \cdot R_{ia_vad}$$

$$V_{cfd_4}(y) := V_{cfd_3}(y) - (y_{17} + y_{16}) \cdot R_{rca_ia}$$

$$V_{cfd_5}(y) := V_{cfd_4}(y) - (y_{18} + y_{19}) \cdot R_{ia_rsa}$$

$$V_{cfd_6}(y) := V_{cfd_3}(y) - (y_{21} + y_{22}) \cdot R_{lca_ia}$$

$$V_{cfd_7}(y) := V_{cfd_6}(y) - (y_{26} + y_{23}) \cdot R_{lsa_lca}$$

$$V_{cfd_8}(y) := V_{cfd_7}(y) - (y_{24} + y_{25}) \cdot R_{da_lsa}$$

-----Auxiliary Current equations-----

$$i_1(y) = y_4 \quad i_2(y) = \frac{y_5 - y_6}{R_{1a}} \cdot \text{hev}(y_5, y_6) \quad i_3(y) = \frac{y_6 - y_8}{R_{1v}} \cdot \text{hev}(y_6, y_8)$$

$$i_5(y) = \frac{y_{40} - y_{49}}{R_{dsb}} \quad i_6(y) = \frac{y_{43} - y_{49}}{R_{dcb}} \quad i_7(y) = \frac{y_{46} - y_{49}}{R_{dvb}}$$

$$i_8(y) = \frac{y_{48} - y_{49}}{R_{1vb}}$$

$$i_9(y) = \frac{y_{49} - y_{50}}{R_{1a}} \cdot \text{hev}(y_{49}, y_{50}) \quad i_{10}(y) = \frac{y_{50} - y_1}{R_{1v}} \cdot \text{hev}(y_{50}, y_1) \quad i_{11}(y) = \frac{y_{37} - y_{49}}{R_{corvb}}$$

APPENDIX B: FIGURES

LVAD Circuit Lumped Model

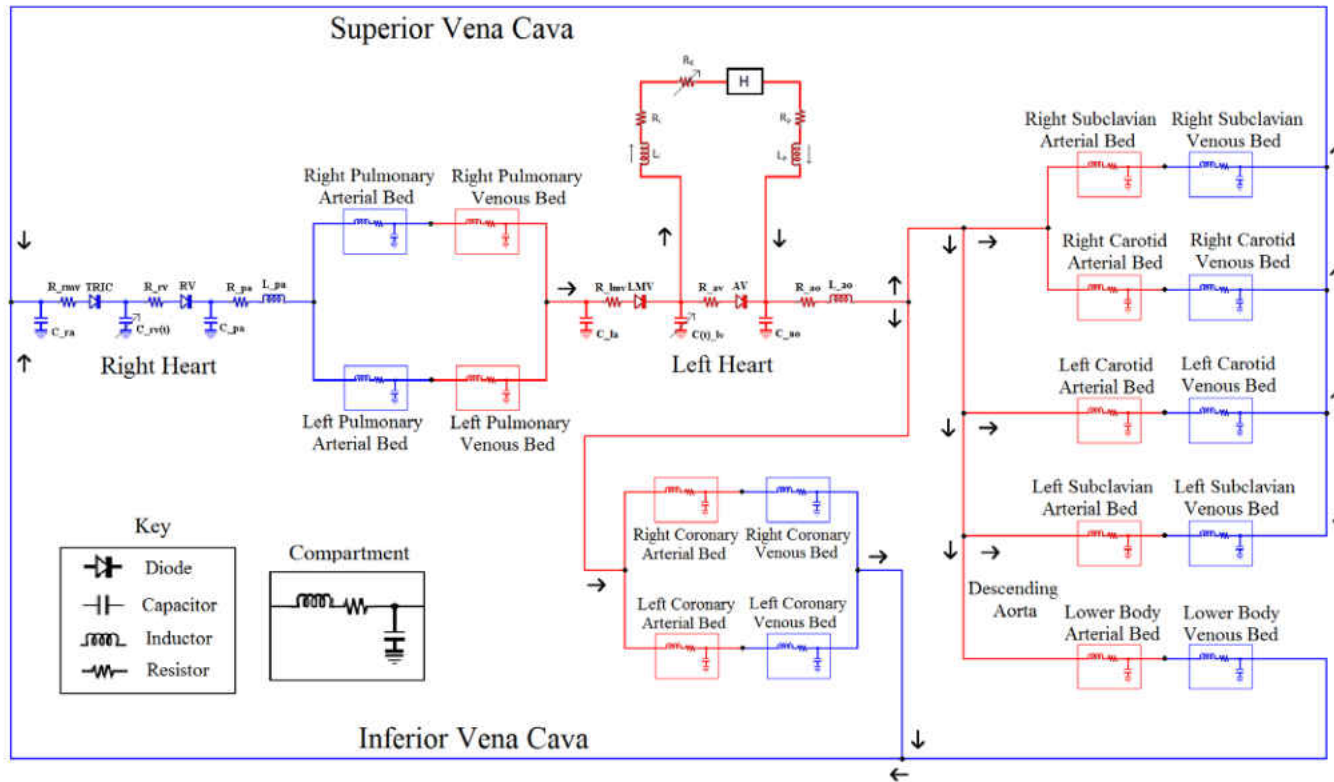


Figure 33 - FULL LVAD circuit LPM

APPENDIX C: TABLES

Table 14 - 2.5mm particle data for each outlet for Intermediate geometry.

run	injected	DA	%	L_Cor	%	L_Vert	%	LCA	%	LSA	%	R_Cor	%	R_Vert	%	RCA	%	RSA	%
1	343	171	49.85	0	0.00	14	4.08	32	9.33	39	11.37	3	0.87	6	1.75	46	13.41	58	16.91
2	348	158	45.40	2	0.57	7	2.01	42	12.07	30	8.62	2	0.57	7	2.01	50	14.37	59	16.95
3	369	176	47.70	2	0.54	3	0.81	45	12.20	39	10.57	3	0.81	2	0.54	48	13.01	50	13.55
4	385	139	36.10	1	0.26	6	1.56	56	14.55	40	10.39	1	0.26	4	1.04	46	11.95	41	10.65
5	337	176	52.23	1	0.30	6	1.78	41	12.17	42	12.46	0	0.00	8	2.37	40	11.87	43	12.76
tot	1782	2	46.0		0.34		2.02		12.12		10.66		0.51		1.52		12.91		14.09
mean			46.26		0.33		2.05		12.06		10.68		0.50		1.54		12.92		14.16
st dev			5.56		0.21		1.09		1.65		1.26		0.33		0.66		0.94		2.45
variance			46.26±5.56		0.33±0.21		2.05±1.09		12.06±1.65		10.68±1.26		0.50±0.33		1.54±0.66		12.92±0.94		14.16±2.45

Table 15 - 2.5mm particle count at cerebral vessels for Intermediate geometry.

run	Vertebrals	%	Carotids	%	Overall	%
1	20	5.83	78	22.74	98	28.57
2	14	4.02	92	26.44	106	30.46
3	5	1.36	93	25.20	98	26.56
4	10	2.60	102	26.49	112	29.09
5	14	4.15	81	24.04	95	28.19
tot		3.54		25.03		28.56
mean		3.59		24.98		28.57
st dev		1.52		1.44		1.27
variance		3.59±1.52		24.98±1.44		28.57±1.27

Table 16 - 3.5mm particle data for each outlet for Intermediate geometry.

run	injected	DA	%	L_Cor	%	L_Vert	%	LCA	%	LSA	%	R_Cor	%	R_Vert	%	RCA	%	RSA	%
1	368	128	34.78	0	0.00	5	1.36	55	14.95	30	8.15	1	0.27	3	0.82	31	8.42	31	8.42
2	341	190	55.72	4	1.17	9	2.64	48	14.08	34	9.97	0	0.00	7	2.05	45	13.20	40	11.73
3	326	161	49.39	4	1.23	11	3.37	50	15.34	41	12.58	3	0.92	7	2.15	52	15.95	43	13.19
4	383	187	48.83	2	0.52	5	1.31	44	11.49	45	11.75	1	0.26	6	1.57	45	11.75	48	12.53
5	377	181	48.01	8	2.12	5	1.33	44	11.67	38	10.08	4	1.06	4	1.06	44	11.67	51	13.53
tot	1795		47.19		1.00		1.95		13.43		10.47		0.50		1.50		12.09		11.87
mean			47.34		1.01		2.00		13.50		10.51		0.50		1.53		12.20		11.88
st dev			6.85		0.72		0.85		1.62		1.54		0.41		0.53		2.44		1.83
variance			47.34±6.85		1.01±0.72		2.00±0.85		13.50±1.62		10.51±1.54		0.50±0.41		1.53±0.53		12.20±2.44		11.88±1.83

Table 17 - 3.5mm particle count at cerebral vessels for Intermediate geometry.

run	Vertebrals	%	Carotids	%	Overall	%
1	8	2.17	86	23.37	94	25.54
2	16	4.69	93	27.27	109	31.96
3	18	5.52	102	31.29	120	36.81
4	11	2.87	89	23.24	100	26.11
5	9	2.39	88	23.34	97	25.73
tot		3.45		25.52		28.97
mean		3.53		25.70		29.23
st dev		1.33		3.19		4.48
variance		3.53±1.33		25.70±3.19		29.23±4.48

Table 18 - 2.5mm particle count at each outlet for Perpendicular geometry.

run	injected	DA	%	L_Cor	%	L_Vert	%	LCA	%	LSA	%	R_Cor	%	R_Vert	%	RCA	%	RSA	%
1	182	119	65.38	1	0.55	0	0	8	4.40	4	2.20	0	0.00	0	0.00	10	5.49	16	8.79
2	125	87	69.60	1	0.80	1	0.8	3	2.40	1	0.80	1	0.80	2	1.60	4	3.20	6	4.80
3	122	78	63.93	1	0.82	0	0	6	4.92	9	7.38	2	1.64	1	0.82	5	4.10	8	6.56
4	175	106	60.57	0	0.00	0	0	8	4.57	6	3.43	2	1.14	0	0.00	8	4.57	5	2.86
5	67	44	65.67	0	0.00	0	0	5	7.46	7	10.45	0	0.00	1	1.49	0	0.00	2	2.99
tot	671		64.68		0.45		0.15		4.47		4.02		0.75		0.60		4.02		5.51
mean			65.03		0.43		0.16		4.75		4.85		0.72		0.78		3.47		5.20
st dev			2.92		0.37		0.32		1.62		3.55		0.64		0.69		1.89		2.25
variance			65.03±2.92		0.43±0.37		0.16±0.32		4.75±1.62		4.85±3.55		0.72±0.64		0.78±0.69		3.47±1.89		5.20±2.25

Table 19 - 2.5mm particle count at cerebral vessels for Perpendicular geometry.

run	Vertebrals	%	Carotids	%	Overall	%
1	0	0.00	18	9.89	18	9.89
2	3	2.40	7	5.60	10	8.00
3	1	0.82	11	9.02	12	9.84
4	0	0.00	16	9.14	16	9.14
5	1	1.49	5	7.46	6	8.96
tot		0.75		8.49		9.24
mean		0.94		8.22		9.16
st dev		0.92		1.53		0.69
variance		0.94±0.92		8.22±1.53		9.16±0.69

Table 20 - 3.5mm particle count at each outlet for Perpendicular geometry.

run	injected	DA	%	L_Cor	%	L_Vert	%	LCA	%	LSA	%	R_Cor	%	R_Vert	%	RCA	%	RSA	%
1	68	36	52.94	0	0.00	0	0.00	2	2.94	4	5.88	0	0.00	1	1.47	2	2.94	0	0.00
2	57	21	36.84	0	0.00	0	0.00	4	7.02	1	1.75	0	0.00	0	0.00	3	5.26	1	1.75
3	126	93	73.81	0	0.00	0	0.00	10	7.94	9	7.14	0	0.00	1	0.79	5	3.97	6	4.76
4	61	46	75.41	0	0.00	0	0.00	4	6.56	2	3.28	0	0.00	0	0.00	2	3.28	4	6.56
5	61	47	77.05	0	0.00	0	0.00	6	9.84	7	11.48	0	0.00	1	1.64	3	4.92	2	3.28
tot	373		49.59		0.00		0.00		5.31		4.69		0.00		0.61		3.06		2.65
mean			63.21		0.00		0.00		6.86		5.91		0.00		0.78		4.07		3.27
st dev			15.83		0.00		0.00		2.26		3.37		0.00		0.70		0.90		2.28
variance			63.21±15.83		0.00±0.00		0.00±0.00		6.86±2.26		5.91±3.37		0.00±0.00		0.78±0.70		4.07±0.90		3.27±2.28

Table 21 - 3.5mm particle count at cerebral vessels for Perpendicular geometry.

run	Vertebrals	%	Carotids	%	Overall	%
1	1	1.47	4	5.88	5	7.35
2	0	0.00	7	12.28	7	12.28
3	1	0.79	15	11.90	16	12.70
4	0	0.00	6	9.84	6	9.84
5	1	1.64	9	14.75	10	16.39
tot		0.61		8.37		8.98
mean		0.78		10.93		11.71
st dev		0.70		2.97		3.02
variance		0.78±0.70		10.93±2.97		11.71±3.02

APPENDIX D: CODES

Coupling Code

```
package macro;

import java.nio.file.*;
import static java.nio.file.StandardCopyOption.*;
import java.nio.file.attribute.*;
import static java.nio.file.FileVisitResult.*;
import java.io.IOException;
import java.util.*;

import star.common.*;
import star.base.neo.*;
import star.vis.*;
import java.io.*;
import java.net.*;

// Note: To get macro commands from the CFD simply hit the record button and save the Java file. Once you are done with the in software commands, hit stop and all the
// commands will be saved in the Java file you created. These commands can be used below.

public class FontanCoupler extends StarMacro
{
    // USER_TODO: Change the following configuration variables; Note that these variables must match the configuration of the RK solver

    // Number of heart cycles to run
    public int num_cycles = 10;

    // Number of time steps per heart cycle (CFD)
    public int steps_per_cycle = 1200;

    // Number of time step per heart cycle (LPM)
    public int LPM_steps_per_cycle = 8000;

    // Heart rate
    public double heart_rate = 80.0;

    // Number of solver iterations per solver timestep (i.e. 50 iterations/time step)
    public int iters_per_step = 250;
    public int iters_per_step_final = 200;

    // Absolute file path of the compiled RK executable

    //public String rkExePath = "New_Fontan_RK/BIN/RK_Fontan.exe";
    public String rkExePath = "C:\\Users\\ra400879\\Desktop\\New_Fontan_RK_Ray\\BIN\\RK_Fontan.exe";
    //public String rkExePath = "share/CERT/Fontan_Models/Baseline_Batch_Testing/New_Fontan_RK/BIN/RK_Fontan.exe.Ink";

    // Absolute file path of the table output by the RK executable
```

```

//public String rkOutputTablePath = "/New_Fontan_RK/BIN/Outputs/Fontan.csv";

//public String rkOutputTablePath = "c:/Users/ra400879/Desktop/New_Fontan_RK_Ray/BIN/Outputs/LVAD.csv";
public String rkOutputTablePath = "/share/CERT/Ray_Thesis/New_Fontan_RK_Ray/BIN/Outputs/LVAD.csv";

// Absolute file path of the sim file
//public String simPath = "/Baseline_Simulation_V2.0/Baseline-V2.2_Copy.sim";
public String simPath = "/share/CERT/Ray_Thesis/StarCCM_Simulation/LVAD_Unsteady_CO_4_1_perpendicular.sim";

//public String simPath = "/share/CERT/Ray_Thesis/StarCCM_Simulation/LVAD_Unsteady_CO_4_1_perpendicular.sim";

// Absolute file path of the table output from Star-CCM+ that is used by the RK solver for coupling
//public String cfdOutputTablePath = "/New_Fontan_RK/BIN/PressOut.csv";
public String cfdOutputTablePath = "C:/Users/ra400879/Desktop/New_Fontan_RK_Ray/BIN/CFDOut.csv";

//public String cfdOutputTablePath = "/share/CERT/Ray_Thesis/New_Fontan_RK/BIN/Outputs/CFDOut.csv";

// USER_TODO: End changing configuration variables

// Calculated time step length
public double dt = 60.0/heart_rate/steps_per_cycle; // (60.0 s)/HR/NUM_STEPS

public void execute()
{
    // Set the time step length based on the value calculated above
    setTimestep();

    for(int i = 0; i < num_cycles; i++)
    {
        runRK();

        // Run a CFD/LPM steps per cycle

        mFile();

        runSim();

        // Output values from Star-CCM+ for coupling
        updateRKInputs();

        // Backup the simulation's state after each cycle
        backupCycle(i);

    }
}

public void setTimestep()
{
    // Set the time step length based on the value calculated above

```



```

Simulation sim = getActiveSimulation();
ImplicitUnsteadySolver unsteadySolver = (ImplicitUnsteadySolver) sim.getSolverManager().getSolver(ImplicitUnsteadySolver.class);

unsteadySolver.getTimeStep().setValue(dt);
}

public void runRK()
{
    try
    {

        // Define the location of the RK solver executable
        File rkExe = new File(rkExePath);

        ProcessBuilder rkp = new ProcessBuilder(rkExe.getAbsolutePath());

        // Define the working directory of the RK solver
        rkp.directory(new File(rkExe.getParent()));

        System.out.println("About to start RK solver");

        Process rkp = rkp.start();

        // This is the waiting function that will wait for your RK Solver to finish before starting the sim

        InputStream in = rkp.getInputStream();
        in.close();
        OutputStream out = rkp.getOutputStream();
        out.close();
        InputStream error = rkp.getErrorStream();
        error.close();
        rkp.waitFor();
        rkp.destroy();

        System.out.println("Finished RK solver");
    }
    catch(Exception e)
    {
        System.out.println("Error while running RK solver: " + e.toString());
    }
}

public static void mFile()
{
    try
    {

```

```

// File (or Directory) to be moved
Path src_Path = Paths.get("c:\\Users\\ra400879\\Desktop\\New_Fontan_RK_Ray\\BIN\\Outputs\\LVAD.csv");

// Destination directory
Path dest_Path = Paths.get("z:\\CERT\\Ray_Thesis\\New_Fontan_RK_Ray\\BIN\\Outputs\\LVAD.csv");

// Move file to a new directory
Files.copy(src_Path, dest_Path, REPLACE_EXISTING);

System.out.println("Move successful");

}

catch (Exception ex)
{
System.out.println(ex);
}
}

public void runSim()
{
Simulation sim = getActiveSimulation();
Solution solution_0 = sim.getSolution();
solution_0.clearSolution(Solution.Clear.History);
System.out.println("History cleared");

// This is where the CFD solver updates its boundary conditions based on the table of outputs that the RK solver writes out, The actual file that the RK solver
puts out needs
// to be set up in the CFD, under Tools.Tables , In this instance the Table is named BCs
FileTable bcs = (FileTable) sim.getTableManager().getTable("LVAD");
bcs.setFileName(rkOutputTablePath);
bcs.extract();

// Run one timestep in the CFD
InnerIterationStoppingCriterion innerItrs = (InnerIterationStoppingCriterion)
(sim.getSolverStoppingCriterionManager().getSolverStoppingCriterion("Maximum Inner Iterations"));

innerItrs.setMaximumNumberInnerIterations(iters_per_step);
sim.getSimulationIterator().step(1);

innerItrs.setMaximumNumberInnerIterations(iters_per_step_final);
sim.getSimulationIterator().run();

}

// Backs up the current version of the simulation in a new folder
// called "<sim's parent directory>- Cycle #"
public void backupCycle(int cycleNum)

```

```

{
    System.out.println("Started backup of cycle #" + cycleNum);
    File simFile = new File(simPath);

    Path srcDir = Paths.get(simFile.getParent());
    Path destDir = Paths.get(simFile.getParent() + String.format("- Cycle %d", cycleNum));

    try
    {
        copyDirRecursive(srcDir, destDir);

        System.out.println("Finished backup of current cycle");
    }
    catch(Exception e)
    {
        System.out.println("Error occured while backing up current cycle: " + e);
    }
}

// Program to update the Lumped model with new resistances for the Lumped parameter model (RK solver)
public void updateRKInputs()
{
    Simulation sim = getActiveSimulation();

    // grabs the Table that starccm creates in the softwares itself. In this instance the name of the table is "PressOut"
    // This PressOut is located in the plots sections of the CFD
    MonitorPlot plot = ((MonitorPlot) sim.getPlotManager().getObject("CFDOut"));

    // takes that table and outputs to a csv file
    plot.export(resolvePath(cfdOutputTablePath), ".");
}

// Recursively copies the contents of srcDir to destDir
public void copyDirRecursive(final Path srcDir, final Path destDir) throws IOException
{
    EnumSet options = EnumSet.of(FileVisitOption.FOLLOW_LINKS);

    if(Files.isDirectory(srcDir))
    {
        Files.walkFileTree(srcDir, options, Integer.MAX_VALUE, new FileVisitor<Path>() {

            @Override
            public FileVisitResult postVisitDirectory(Path dir, IOException exc) throws IOException
            {
                return FileVisitResult.CONTINUE;
            }
        });
    }
}

```

```

@Override
public FileVisitResult preVisitDirectory(Path dir, BasicFileAttributes attrs)
{
    CopyOption[] opt = new CopyOption[]{COPY_ATTRIBUTES, REPLACE_EXISTING};

    Path newDirectory = destDir.resolve(srcDir.relativeTo(dir));

    try
    {
        Files.copy(dir, newDirectory, opt);
    }
    catch(FileAlreadyExistsException x)
    {
    }
    catch(IOException x)
    {
        return FileVisitResult.SKIP_SUBTREE;
    }

    return CONTINUE;
}

@Override
public FileVisitResult visitFile(Path file, BasicFileAttributes attrs) throws IOException
{
    copyFile(file, destDir.resolve(srcDir.relativeTo(file)));
return CONTINUE;
}

@Override
public FileVisitResult visitFileFailed(Path file, IOException exc) throws IOException
{
    return CONTINUE;
}

});
}

public static void copyFile(Path src, Path dest) throws IOException
{
    CopyOption[] options = new CopyOption[]{REPLACE_EXISTING, COPY_ATTRIBUTES};
    Files.copy(src, dest, options);
}
}

```

LIST OF REFERENCES

- [1] Osorio, A.F., Osorio, R., Ceballos, A., Tran, R., Clark, W., Divo, E.A., Argueta-Morales, I.R., Kassab, A.J., and DeCampli, W.M., "Computational Fluid Dynamics Analysis of Surgical Adjustment of Left Ventricular Assist Device Implantation to Minimize Stroke Risk," *Computer Methods in Biomechanics and Biomedical Engineering*, 2013, Vol. 16, no. 4-6, pp. 622 – 638.
- [2] I. Ricardo Argueta-Morales, Reginald Tran, William Clark, Eduardo Divo, Alain Kassab, William M. DeCampli, "Use of Computational Fluid Dynamics (CFD) to Tailor the Surgical Implantation of a Ventricular Assist Device (VAD): A Patient-Specific Approach to Reduce Risk of Stroke," Presented at the Surgical Forum program of the American College of Surgeons 96th Annual Clinical Congress, October 3-7, 2010, Washington, DC. (Abstract SF2010-10094), *Journal of the American College of Surgeons*, Vol. 211, No. 3, Sept. 2010, p. S26.
- [3] C.A. Taylor, J.D. Humphrey, "Open problems in computational vascular biomechanics: Hemodynamics and arterial wall mechanics", *Comput. Methods Appl. Mech. Engrg.*, Vol. 198, Feb. 2009, pp. 3514–3523.
- [4] C.A. Taylor and C.A. Figueroa, "Patient-Specific Modeling of Cardiovascular Mechanics", *Annu. Rev. Biomed. Eng.*, Vol. 11, Apr. 2009, pp. 109–134.
- [5] Takami Yamaguchi, Takuji Ishikawa, Y. Imai, N. Matsuki, Mikhail Xenos, Yuefan Deng, And Danny Bluestein, "Particle-Based Methods for Multiscale Modeling of Blood Flow in the Circulation and in Devices: Challenges and Future Directions",

Annals of Biomedical Engineering, Vol. 38, No. 3, March 2010 (© 2010) pp. 1225–1235.

[6] M. Toloui, B. Firoozabadi, M.S. Saidi, “A numerical study of the effects of blood rheology and vessel deformability on the hemodynamics of carotid bifurcation”, *Scientia Iranica*, Vol. 19, Issue 1, Feb. 2012, pp. 119-126.

[7] S. Baek and J.D. Humphrey, “Computational Modeling of Growth Biological Soft Tissues: Application to Arterial Mechanics”, *Computational Modeling in Biomechanics*, DOI 10.1007/978-90-481-3575-2 8, © Springer Science+Business Media B.V. 2010.

[8] Faragallah, G., Wang, Y., Divo, E., & Simaan, M. (n.d.). A new control system for left ventricular assist devices based on patient-specific physiological demand. *Inverse Problems in Science and Engineering*, 721-734.

[9] Argueta-Morales, Ricardo, Reginald Tran, Andres Ceballos, William Clark, Ruben Osorio, Eduardo A. Divo, Alain J. Kassab, and William M. DeCampi. "Mathematical Modeling of Patient-Specific Ventricular Assist Device Implantation to Reduce Particulate Embolization Rate to Cerebral Vessels." *Journal of Biomechanical Engineering* 136.071008 (2014): 1-8. Print.

[10] Travis, A., G. Giridharan, G. Pantalos, R. Dowling, S. Prabhu, M. Slaughter, M. Sobieski, A. Undar, D. Farrar, and S. Koenig. "Vascular Pulsatility In Patients With A Pulsatile- Or Continuous-flow Ventricular Assist Device." *The Journal of Thoracic and Cardiovascular Surgery*: 517-24. Print.